*Chemistry – A European Journal*

ChemEurJ Chemistry Europe European Chemical Societies Publishing

RESEARCH ARTICLE

# Coordination Complexes and Polymers of Novel Hybrid Tetrazole-Triazole-Pyrazole Ligands: Synthesis, Structural Characterization, and Biological Evaluation

Yousra Bahjou[1,2] | Youssef Draoui[1] | Smaail Radi[1] | Koen Robeyns[2] | Weiyang Li[2] | Haralampos N. Miras[3] | Marilena Ferbinteanu[4] | Aurelian Rotaru[5] | Hannah Bittner[6] | Michael A. Jakupec[6] | Christian Kowol[6] | Olivera Cvetković[7] | Mariusz Wolff[7] | Yann Garcia[2]

[1]LCAE, Department of Chemistry, Faculty of Science, University Mohamed I, Oujda, Morocco | [2]Institute of Condensed Matter and Nanosciences, Molecular Chemistry, Materials and Catalysis (IMCN/MOST), Université Catholique De Louvain, Louvain-la-Neuve, Belgium | [3]School of Chemistry, Joseph Black Building, University of Glasgow, Glasgow, UK | [4]Inorganic Chemistry Department, Faculty of Chemistry, University of Bucharest, Bucharest, Romania | [5]Department of Electrical Engineering and Computer Science & Research Center MANSiD, Stefan Cel Mare University, Suceava, Romania | [6]Institute of Inorganic Chemistry, Faculty of Chemistry, University of Vienna, Wien, Austria | [7]Institute of Functional Materials and Catalysis, Faculty of Chemistry, University of Vienna, Wien, Austria

**Correspondence:** Smaail Radi (s.radi@ump.ac.ma) | Yann Garcia (yann.garcia@uclouvain.be)

**Received:** 9 July 2025 | **Revised:** 24 December 2025 | **Accepted:** 29 December 2025

**Keywords:** antitumor | coordination compounds | pyrazole | tetrazole | triazole

## ABSTRACT

New series of triazole/pyrazole and tetrazole/triazole/pyrazole ligands were synthesized and coordinated with various transition metals to yield a diverse library of 14 complexes. All compounds were fully characterized by elemental analysis, mass spectrometry, powder X-ray diffractometry, and a range of spectroscopic techniques ($^{1}$H NMR, $^{13}$C NMR, FT-IR, and UV–visible diffuse reflectance). The crystal and molecular structures were elucidated via single-crystal X-ray diffraction, and their supramolecular features were explored through Hirshfeld surface analysis. The $^{57}$Fe Mössbauer and magnetic SQUID measurements confirmed the high-spin nature of the $Fe^{II}$ complex **1**. In the three human cancer cell lines, most metal complexes are somewhat more cytotoxic than the inactive ligands, with Co(II) complexes **2** and **8** being the most potent in two of the cell lines (with $IC_{50}$ values in the two-digit micromolar range). Overall, this study highlights how blending tetrazole/triazole/pyrazole ligands with transition metals can lead to coordination compounds with potential in anticancer research, as a proof of concept. These results add valuable insight to the expanding field of metal-based therapeutics and could help guide the development of next-generation, more effective agents.

## 1 | Introduction

Azoles are five-membered heterocyclic compounds with at least two heteroatoms, one of which is nitrogen. These compounds, along with their derivatives, are recognized as pharmaceutically and medically important drug scaffolds due to their biological activity [1].

In coordination chemistry, azoles are extensively studied for their ability to act as versatile ligands for metal ions. Their ability to adopt various coordination modes—such as monodentate, bridging, and chelating—facilitates the formation of metal complexes with a range of nuclearities, from mononuclear to polynuclear species, including coordination polymers and metal-organic frameworks (MOFs) [2–5]. These complexes exhibit

unique properties, such as spin crossover behavior (e.g., in $Fe^{II}$ complexes) [6, 8], antimicrobial and antioxidant activity (e.g., in $Cu^{II}$ and $Ni^{II}$ complexes) [9–16], corrosion inhibition activity (e.g., in $Co^{II}$ and $Ni^{II}$ complexes) [17], and photoluminescence (e.g., in $Zn^{II}$ and $Cd^{II}$ complexes) [3]. Furthermore, azole-based metal complexes are applied in catalysis [18], chemical sensing [19–21], and materials science, demonstrating their significance in both fundamental and applied chemistry [22, 23].

In recent decades, drug discovery has emerged as a crucial component of medical research. The extensive chemical diversity found in heterocyclic compounds has garnered significant global interest. Notably, nitrogen-based heterocycles such as pyrazole derivatives exhibit a wide range of biological activities and hold considerable potential in pharmaceutical applications, owing to their distinctive chemical frameworks [24, 25]. Their biological activity further supports their potential as promising candidates for anticancer applications across various cell types. A wide range of azole derivatives have been developed with the aim of inhibiting tumor-associated proteins such as kinases, [26, 27] microtubule-associated proteins [28], topoisomerases [29], and Cyclooxygenase-2 [30]. These compounds have been extensively evaluated for their anticancer properties, demonstrating significant activity in preclinical studies. Some of these derivatives have shown promising results and have progressed into clinical trials for the treatment of various aggressive cancers [31, 32].

On the other hand, the coordination compounds integrating transition metals in these heterocyclic compounds, can further enhance or even add nonexisting antitumor properties to the hybrid system and thus open unlimited possibilities for investigation and optimization [33, 34]. For instance, two new triazole cadmium coordination complexes have been reported for their antitumor activities against triple negative breast cancer, showing positive selectivity index toward the MDA-MB-468 Cell Line even when the ligands initially were inactive [35]. Moreover, a new binuclear $Ru^{II}$ tetrazole coordination complex was also reported for its selectivity and high cytotoxicity against HeLa and MCF-7 cell lines [36].

Driven by the broad success of azole-based heterocycles in anticancer research, our group has designed new hybrid ligands, including triazole/pyrazole **L1**, tetrazole/triazole/pyrazole **HL2**, pyrazole **L3**, and tetrazole/pyrazole **HL4**, and investigated their coordination behavior with metal salts. The resulting coordination complexes, including $[Fe(\mathbf{L1})_3](ClO_4)_2$ (**1**), $[Co(\mathbf{L1})_3](ClO_4)_2$ (**2**), $[Ni(\mathbf{L1})_3](ClO_4)_2$ (**3**), $[Cu(\mathbf{L1})_2(NO_3)]NO_3$ (**4**), $[Cd(\mathbf{L1})Cl_2]_n$ (**5**), $[Ni(\mathbf{HL2})_3](ClO_4)_2$ (**6**), $[Cu(\mathbf{HL2})Cl_2]$ (**7**), $[Co(MeOH)_2(\mathbf{L3})_2](ClO_4)_2$ (**8**), $[Cu(MeCN)_2(\mathbf{L3})_2](ClO_4)_2$ (**9**), $\{[Cu(\mathbf{HL4})_2]\cdot 2H_2O\}_n$ (**10**), $[Cu(\mathbf{HL4})Cl]_n$ (**11**), $[Ni(\mathbf{L5})_3](ClO_4)_2$ (**12**), $[Ni(\mathbf{HL6})_3](ClO_4)_2$ (**13**), $[Ni_2(\mathbf{HL6})(\mathbf{L6})Cl_3]$ (**14**), were characterized by elemental analysis, mass spectrometry, FT–IR and UV–visible diffuse reflectance spectroscopies, as well as powder X-ray diffraction analysis. The cytotoxicity of these new compounds was tested against three types of human cell lines including A549, CH1/PA-1, and SW480 relative to lung carcinoma, ovarian teratocarcinoma, and colon adenocarcinoma respectively, three of the most prevalent and clinically challenging cancers worldwide. Despite their widespread use individually, comparative studies involving metal-based compounds across all three have been relatively limited in literature. By including these distinct models, we aim to provide a broader perspective on the spectrum of activity, while contributing novel insights into underexplored therapeutic avenues, particularly for ovarian germ cell tumors. Furthermore, the Hirshfeld surface and 2D fingerprint calculations of these newly synthesized compounds were performed and discussed.

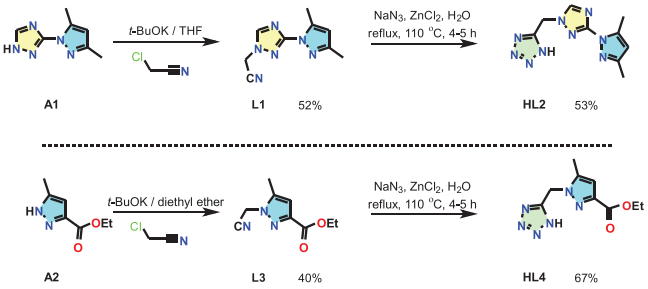


**SCHEME 1** | Synthesis of **L1**, **HL2**, **L3,** and **HL4**.

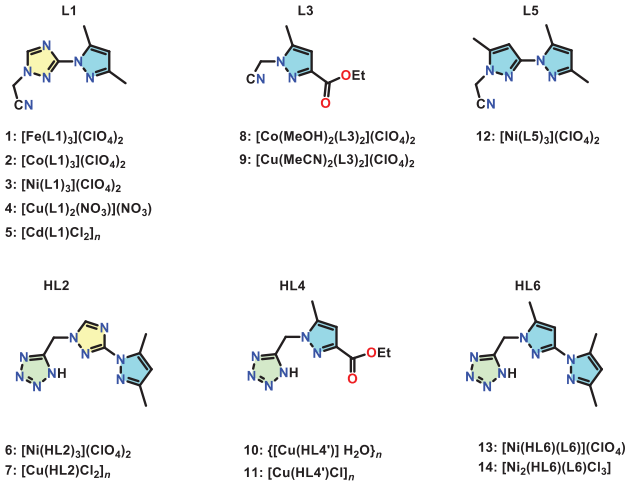


**SCHEME 2** | Coordination compounds **1–14** studied in this work.

## 2 | Results and Discussion

### 2.1 | Synthesis and Spectroscopic (FT–IR, UV–Vis DRS) Characterization

Alkylation of 3-(3,5-dimethyl-1*H*-pyrazol-1-yl)-1*H*-1,2,4-triazole (**A1**) and ethyl 5-methyl-1*H*-pyrazole-3-carboxylate (**A2**) with 2-chloroacetonitrile in the presence of potassium *tert*-butoxide (*t*-BuOK) in either THF or diethyl ether resulted in the formation of new products 2-(3-(3,5-dimethyl-1*H*-pyrazol-1-yl)-1*H*-1,2,4-triazol-1-yl)acetonitrile (**L1**) and ethyl 1-(cyanomethyl)-5-methyl-1*H*-pyrazole-3-carboxylate (**L3**). **L1** was purified by column chromatography on silica gel, using hexane and ethyl acetate (2:8) as eluent. Cyclization reaction of **L1** and **L3**, respectively, with $NaN_3$ in the presence of a $ZnCl_2$ catalyst in distilled $H_2O$ yielded 5-((3-(3,5-dimethyl-1*H*-pyrazol-1-yl)-1*H*-1,2,4-triazol-1-yl)methyl)-1*H*-tetrazole (**HL2**) and ethyl 1-((1*H*-tetrazol-5-yl)methyl)-5-methyl-1*H*-pyrazole-3-carboxylate (**HL4**) (Scheme 1). Scheme 2

**L1**, **HL2**, **L3,** and **HL4** were reacted with metal salts ($Fe(ClO_4)_2{\cdot}H_2O$, $Co(ClO_4)_2{\cdot}6H_2O$, $Ni(ClO_4)_2{\cdot}6H_2O$, $Cu(ClO_4)_2{\cdot}6H_2O$, $Cu(NO_3)_2{\cdot}3H_2O$ or $CdCl_2$) in a 3:1 ligand-to-metal ratio in methanol. Slow diffusion of diethyl ether into the methanol solutions of the resulting metal complexes produced single crystals (**1–5**, **8,** and **9**) suitable for X-ray diffraction analysis. Acetonitrile was used in the reaction of $Co(ClO_4)_2{\cdot}6H_2O$ with **L3**.

**HL2** and **HL4**, dissolved in a 5% perchloric or hydrochloric acid solution, were mixed with $Ni(ClO_4)_2{\cdot}6H_2O$, $Cu(ClO_4)_2{\cdot}6H_2O$, and anhydrous $CuCl_2$ at a 3:1 ligand-to-metal ratio. For **HL2** with $CuCl_2$, a 1:1 ratio was used. Slow evaporation of the resulting solutions at ambient temperature yielded single crystals (**6, 7, 10,** and **11**) suitable for X-ray diffraction analysis. During these reactions, **HL4** underwent hydrolysis under the reaction conditions, resulting in **HL4'**.

**L5**, **HL6,** and complex **12** were synthesized following the literature procedure.[80]

$Ni(ClO_4)_2{\bullet}6H_2O$, $NiCl_2{\bullet}6H_2O$ and **HL6** were dissolved in 5% perchloric or hydrochloric acid, respectively, and mixed at a 1:2 metal-to-ligand ratio. The mixture was stirred, and slow evaporation led to the formation of complexes **13** and **14**.

The molecular identity of the organic ligands and their metal complexes was confirmed by mass spectrometry, which provided mass-to-charge ratios and fragmentation patterns consistent with the expected structures. The elemental composition of the polycrystalline powders, determined by elemental analysis, closely matches the expected values based on the single-crystal structure, confirming the purity of the synthesized compounds. PXRD studies confirm the phase purity of the polycrystalline powder samples obtained by grinding single crystals of **1–11** and **14** showing good agreement between the experimental and simulated patterns derived from the single-crystal structure determination (Figures S11–S15). Additionally, sharp and well-defined peaks observed in the PXRD patterns show that the powder samples are highly crystalline, further supporting the accuracy of the phase purity results.

The FT-IR spectra of **L1** and **L3** exhibit distinct bands at 3100, 2990, 2939, and 2926 $cm^{-1}$ (**L1**) and 3142, 2982, and 2939 $cm^{-1}$ (**L3**), attributed to the asymmetric and symmetric stretching vibrations of the C—H bonds of the triazole and pyrazole rings and the tethered $CH_2$ and $CH_3$ groups. A band at 2353 $cm^{-1}$ (**L1**) and 2384 $cm^{-1}$ (**L3**) corresponds to the stretching vibration of the nitrile (C≡N) group. For ligands **HL2** and **HL4**, stretching vibrations of the N—H, C—H, C═C, and N═N bonds were observed at 3370, 3132, 3102, 1599, and 1518 $cm^{-1}$ (**HL2**) and 3158, 3007, 2938, 1597, 1464, and 1435 $cm^{-1}$ (**HL4**) (Figures S1–S5). Most prominent vibration modes associated with the in-plane deformations of the ligand scaffold of **L1** and **L3** could be observed at 1595 and 1557 $cm^{-1}$, as well as 1449 $cm^{-1}$, respectively. The same could be noted for a sharp band at 1422 $cm^{-1}$ in **HL2** and 1368 and 1290 $cm^{-1}$ in **HL4**. Additionally, C═O stretching bands associated with the ester groups in **L3** and **HL4** were observed at 1709 $cm^{-1}$ and 1740 $cm^{-1}$, respectively. In the FT-IR spectra of metal complexes **1–14**, the positions of these bands were slightly shifted, suggesting coordination of the ligands with the metal ions. The FT-IR spectra of the metal complexes (**1**, **2**, **3**, **6**, **8**, **9**, **12**, **13**, and **4**) confirmed the presence of non-coordinated perchlorate ($ClO_4^-$) and nitrate ($NO_3^-$) anions. The sharp peaks of the characteristic asymmetric stretching mode of the uncoordinated perchlorate anion could be identified at around 1078 $cm^{-1}$ and 621 $cm^{-1}$ [37]. The absence of an additional band at around 650 $cm^{-1}$ further serves to indicate the lack of perchlorate coordination to the metal center. On the other hand, the free and the bidentate nitrate of the metal complex **4** could be identified through the presence of bands at 1350 and 1107 $cm^{-1}$, and 1279 and 1013 $cm^{-1}$, commonly attributed to their asymmetric and symmetric stretching vibrations, respectively [38–40]. The FT-IR spectra of the metal complexes indicated coordination of methanol (MeOH) and acetonitrile (MeCN) to the metal centers, as evidenced by the shifts in the characteristic absorption bands. The O—H stretch of MeOH, typically observed around 3680 $cm^{-1}$ [41] exhibited a shift to lower wavenumbers upon coordination, suggesting interaction with the metal ion. Similarly, the C≡N stretch of MeCN, usually found at 2267 $cm^{-1}$ [42], also showed a shift, further confirming its coordination to the metal center. These spectral changes provide direct evidence of the involvement of MeOH and MeCN in the coordination sphere of the metal ions.

The UV-Vis spectra of ligands **L1**, **HL2**, **L3**, **HL4**, and **HL6** exhibited an absorption band at approximately 230 nm, accompanied by a weaker band around 243 nm, which are attributed to $\pi\rightarrow\pi^*$ and $n\rightarrow\pi^*$ electronic transitions, respectively (Figures S6–S10). When compared to the UV-Vis spectra of complexes **1–11** and **14**, the absorption maxima corresponding to intra-ligand $\pi\rightarrow\pi^*$ transitions showed a slight red shift, likely due to the increased conjugation within the ligand framework, leading to a significant increase in the intensity of the strongest absorption peaks. Additionally, the absorption bands observed in the range of 250–340 nm are assigned to ligand-to-metal charge transfer (LMCT) transitions.

## 2.2 | Single Crystal X-ray Diffraction Analysis

Tables S2–S3 list the crystal data and structure refinement parameters, while the selected bond distances and angels are showed in Tables S5–S16.

## 2.3 | Mononuclear $M^{II}$ Complexes 1–3 and 6

Complexes **1–3** crystallize in the triclinic system with the space group *P* –1, while complex **6** adopts the trigonal crystal system with space group R –3, forming mononuclear species of the general formula $[M(\mathbf{L1})_3](ClO_4)_2]$ (M = $Fe^{II}$ (**1**), $Co^{II}$ (**2**), $Ni^{II}$ (**3**)) and $[Ni(\mathbf{HL2})_3](ClO_4)_2$ (**6**). The asymmetric unit of complexes **1–3** and **6** consists of a metal ion coordinated to three bidentate **L1** ligands and two noncoordinated perchlorate ($ClO_{4-}$) anions (Figure 1). In complexes **1–3** and **6**, three $N_{trz}$ atoms as well as three $N_{pz}$ atoms are arranged in a *facial* configuration.

The metal ions in these complexes adopt a distorted $MN_6$ octahedral geometry, with the $\Sigma$ parameter increasing from 74.3° for **3** and 74.2° for **6** to 90.9° for **2** and 97.7° for **1**. The average "bite" angles ∠N–M–N show a decreasing trend: 77.9° for **3**, 77.9° for **6**, 75.7° for **2**, and 74.6° for **1**.

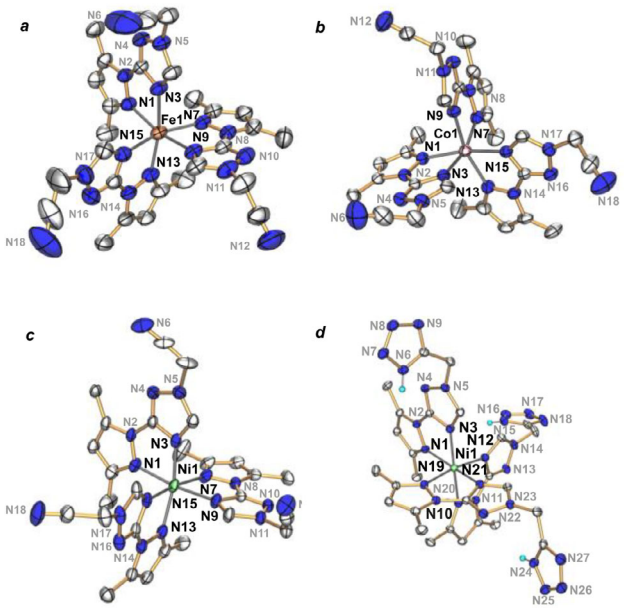


**FIGURE 1** | Molecular structure of: (**a**) $[Fe(\mathbf{L1})_3](ClO_4)_2$ (**1**), (**b**) $[Co(\mathbf{L1})_3](ClO_4)_2$ (**2**), (**c**) $[Ni(\mathbf{L1})_3](ClO_4)_2$ (**3**), and (**d**) $[Ni(\mathbf{HL2})_3](ClO_4)_2$ (**6**). Hydrogen atoms and counter anions $ClO_{4-}$ in **a–d** were omitted for clarity.

The average M–$N_{trz}$ and M–$N_{pz}$ bond lengths are as follows:

2.166(3) and 2.192(3) Å for **1** (M = Fe);
2.115(2) and 2.171(2) Å for **2** (M = Co);
2.069(2) and 2.122(1) Å for **3** (M = Ni);
2.061(8) and 2.114(8) Å for **6** (M = Ni) (Tables S5–S7 and S10).

These bond lengths follow the expected trend based on ligand field theory, decreasing in the order $Ni^{II} < Co^{II} < Fe^{II}$ due to the increasing field strength of the metal ions.

For the $Fe^{II}$ complex **1**, the Fe—N bond lengths determined at ambient temperature are in agreement with those expected for a high-spin (HS) electronic configuration [43, 44]. $^{57}$Fe Mössbauer spectroscopy exhibits a quadrupole doublet typical of HS $Fe^{II}$ ions, with an isomer shift $\delta = 1.05(1)$ mm·s$^{-1}$ and a quadrupole splitting $\Delta E_Q = 1.57(2)$ mm«s$^{-1}$ (Figure S6). Given the potential of the $[FeN_6]^{2+}$ coordination sphere, incorporating pyrazole-triazole ligands, to exhibit spin crossover behavior [45], a cooling experiment was conducted to investigate the possible occurrence of a low-spin (LS) state. However, no color change was observed upon cooling to liquid nitrogen temperatures, suggesting the stabilization of the HS state. SQUID magnetometry measurements down to 2.5 K (Figure S7) confirmed this behavior, demonstrating the paramagnetic character of **1**, consistent with the HS ground state.

## 2.4 | $Cu^{II}$ Complex 4

According to the X-ray analysis, the complex $[Cu(\mathbf{L1})_2(NO_3)]NO_3$ (**4**) crystallizes in the monoclinic space group $P\,1\,2_1/n\,1$. The $Cu^{II}$ ion is coordinated by four nitrogen atoms from two bidentate **L1** ligands and two oxygen atoms from a single nitrate ion, which

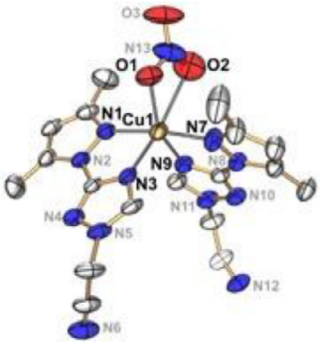

**FIGURE 2** | Molecular structure of $[Cu(\mathbf{L1})_2(NO_3)]NO_3$ (**4**). Counter anion $NO_3^-$ was omitted for clarity.

**TABLE 1** | Parameters used for assigning nitrate coordination modes [46] and parameters of the coordinated nitrate group in the $[Cu(\mathbf{L1})_2(NO_3)]^+$ cation of complex **4**.

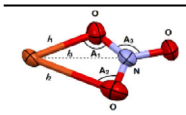

| Empty Cell | Monodentate | Anisobidentate | Bidentate | Complex 3 |
|---|---|---|---|---|
| $l_2$–$l_1$ (Å) | > 0.6 | 0.3–0.6 | < 0.3 | 0.593 |
| $A_1$–$A_2$ (°) | > 28 | 14–28 | < 14 | 27.98 |
| $l_3$–$l_2$ (Å) | < 0.1 | 0.1–0.2 | > 0.2 | 0.08 |
| $A_3$ (°) | < 162 | 162–168 | > 168 | 159.82 |

binds in an anisobidentate mode (Figure 2, Table 1). Within the coordination sphere, two $N_{trz}$ atoms are positioned *cis* to one another, while two $N_{pz}$ atoms occupy the *trans* positions. The copper center adopts a $CuN_4O_2$ distorted octahedral coordination geometry with a $\Sigma$ parameter of 135.0°. The average "bite" angle ∠N—Cu—N is 79.0°. The bond lengths between copper and the nitrogen donor atoms are consistent with typical values for $Cu^{II}$ complexes, with average Cu—$N_{trz}$ and Cu—$N_{pz}$ bond lengths of 2.099(3) and 2.002(3) Å, respectively. The Cu—O bond lengths are 2.018(3) and 2.611(4) Å (Table S8). In the outer coordination sphere, one noncoordinated nitrate anion (acting as a counterion) and one ethanol solvent molecule are present.

## 2.5 | Coordination Polymers 5 and 7

Complex **5** is a coordination polymer with the formula $[Cd(\mathbf{L1})Cl_2]_n$, crystallizing in the monoclinic system with space group $I\,2/c$. The asymmetric unit contains one $Cd^{II}$ ion, one **L1** ligand and three chloride ions. (Figure 3). Neighboring $Cd^{II}$ ions are bridged by two $\mu$-Cl chloride ions, forming an infinite –Cd–Cl2–Cd–Cl2– ribbon chain running along the *a* axis. The Cd···Cd distances between the Cd atoms in the chain are 3.790 and 3.883 Å, respectively. Each $Cd^{II}$ center is coordinated by two nitrogen atoms of the **L1** ligand in the *cis* positions and four chloride ions in the remaining positions, adopting a slightly distorted $CdN_2Cl_4$ octahedral geometry, with a $\Sigma$ parameter of 68.8°. The values of mean Cd—N and Cd—Cl

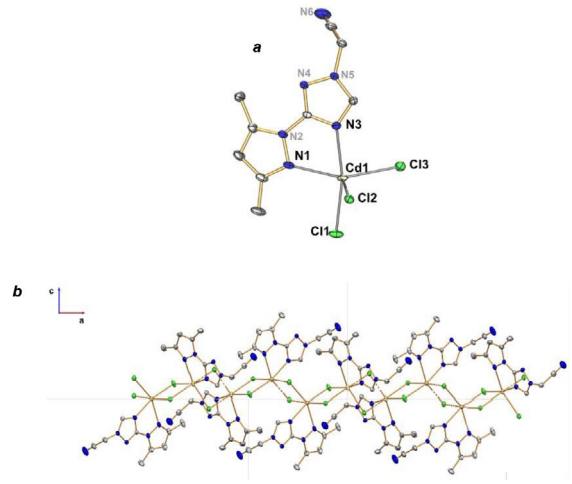


**FIGURE 3** | (a) Molecular structure of $[Cd(\mathbf{L1})Cl_2]_n$ (**5**). (b) A polymeric chain in the structure of $[Cd(\mathbf{L1})Cl_2]_n$.

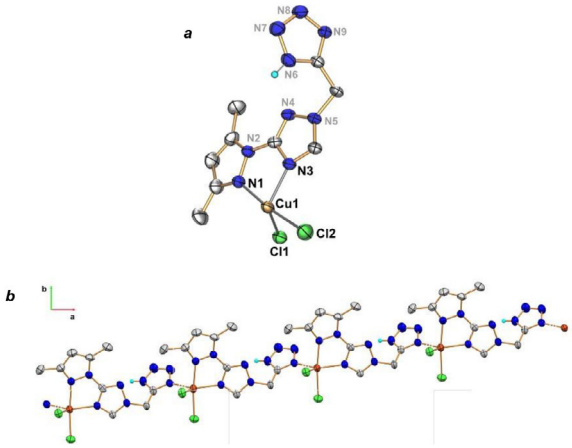


**FIGURE 4** | **(a)** Molecular structure of $[Cu(\mathbf{HL2})Cl_2]_n$ (**7**). (**b**) A polymeric chain in the structure of $[Cu(\mathbf{HL2})Cl_2]_n$.

bonds are 2.4020(8) and 2.6164(2) Å, respectively (Table S9). The **L1** ligand, acting as a bidentate ligand, coordinates to the $Cd^{II}$ center forming a five-membered ring, with a "bite" angle ∠N(1)—Cd(1)—N(3) of 68.91(2)°. The ∠Cl—Cd—Cl angles range from 92.926(7) to 98.057(11)°, and the ∠Cd–Cl–Cd angles vary from 84.257(8) and 106.326(5)°. The planes of the Cd($\mu$-Cl)$_2$Cd cycles in the chain are inclined at an angle of 76.66° to each other, rather than being perpendicular.

Coordination polymer **7**, with the formula $[Cu(\mathbf{HL2})Cl_2]_n$, crystallizes in the monoclinic system with the space group $P\,21/n$. The asymmetric unit contains one $Cu^{II}$ metal center, one **HL2** ligand and two chloride ions ($Cl^-$) (Figure 4). The **HL2** ligand bridges two $Cu^{II}$ ions, resulting in the formation of a 1D coordination polymer that extends along the $a$-axis of the unit cell. The distance between adjacent $Cu^{II}$ ions is 9.074 Å. The $Cu^{II}$ ions are coordinated to **HL2** in two distinct modes: bidentate through N(3) of the triazole ring and N(1) of the pyrazole ring, and monodentate through N(9) of the tetrazole ring. Each $Cu^{II}$ center adopts a trigonal-bipyramidal coordination geometry, with the coordination environment characterized by an Addison $\tau_5$ value

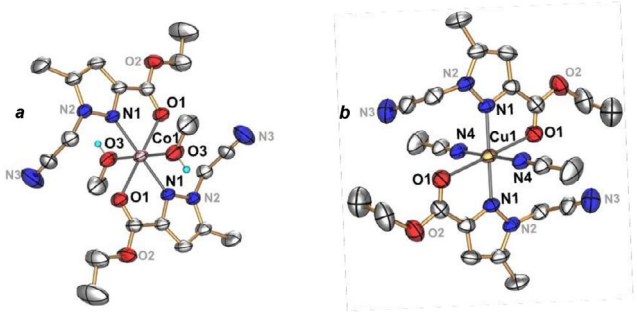


**FIGURE 5** | Molecular structures of $[Co(MeOH)_2(\mathbf{L3})_2](ClO_4)_2$ (**8**) (**a**) and $[Cu(MeCN)_2(\mathbf{L3})_2](ClO_4)_2$ (**9**) (**b**).

of 0.61 indicating a geometry closer to trigonal-bipyramidal (TBP) ($\tau_5 = |\beta-\alpha|/60$, where $\beta$ and $\alpha$ variables are the two greatest coordinate angles X—Cu—X angles of the $CuX_5$ polyhedron; $\tau_5 = 0$ for ideal square-pyramidal geometry with $C_{4v}$ symmetry; $\tau_5 = 1$ for ideal trigonal-bipyramidal geometry with $D_{3h}$ symmetry) [47]. The "bite" angle of the chelating ligand, ∠N(3)—Cu—N(1), is 79.4°. The Cu—N(3) and Cu—N(1) bond lengths differ slightly, with values of 2.016(4) and 2.041(4) Å, respectively (Table S11). The two chloride ions are coordinated in a *cis* arrangement with respect to one another. The equatorial Cu(1)—Cl(2) distance is 2.252(2) Å, which is shorter than the apical Cu(1)—Cl(1) bond length [2.479(2)Å]. The latter is attributed to the Jahn–Teller effect of the $d^9$ electron configuration. The ∠Cl(1)—Cu—Cl(2) angle is 97.35°.

## 2.6 | $M^{II}$ Complexes 8 and 9

Complexes $[Co(MeOH)_2(\mathbf{L3})_2](ClO_4)_2$ (**8**) and $[Cu(MeCN)_2(\mathbf{L3})_2](ClO_4)_2$ (**9**) crystallize in the monoclinic system, with space groups $P2_1/n$ and $C2/c$ for complex **8** and **9**, respectively. The asymmetric unit of each complex contains one metal center, one bidentate **L3** ligand, one solvent molecule (methanol in **8** and acetonitrile in **9**), and one perchlorate counterion (Figure 5). In the X-ray structures of both complexes, the two **L3** ligands coordinate to the metal ion through one nitrogen and one oxygen atom, forming five-membered chelate rings. The "bite" angles of the chelating ligands, ∠N(1)—M—O(1), are 76.48(10)° for **8** and 75.52(6)° for **9** (Tables S12 and S13). These ligands lie in the equatorial plane, with the nitrogen atoms *trans* to each other, as well as the oxygen atoms. The $M^{II}$ ions in both complexes adopt distorted octahedral geometries with the $\Sigma$ parameters being 64.1° for **8** and 68.5° for **9** (Table S1). The axial positions of the coordination sphere are occupied by two solvent molecules, methanol in the case of $[Co(MeOH)_2(\mathbf{L3})_2]^{2+}$ and acetonitrile in $[Cu(MeCN)_2(\mathbf{L3})_2]^{2+}$. The Co—N(1) bond length in $[Co(MeOH)_2(\mathbf{L3})_2](ClO_4)_2$ is 2.103(3) Å, whereas the Cu—N(1) and Cu—$N(4)_{MeCN}$ bond lengths in $[Cu(MeCN)_2(\mathbf{L3})_2](ClO_4)_2$ are 2.0040(14) and 1.9751(17) Å, respectively. These bond lengths are consistent with the expected values for $Co^{II}$ and $Cu^{II}$ complexes, respectively [48–51]. Figure 6

## 2.7 | $Cu^{II}$ Coordination Polymers 10 and 11

In the coordination polymer $\{[Cu(\mathbf{HL_4}')]\cdot H_2O\}_n$ (**10**), crystallizing in the triclinic system P–1, the $Cu^{II}$ center is located

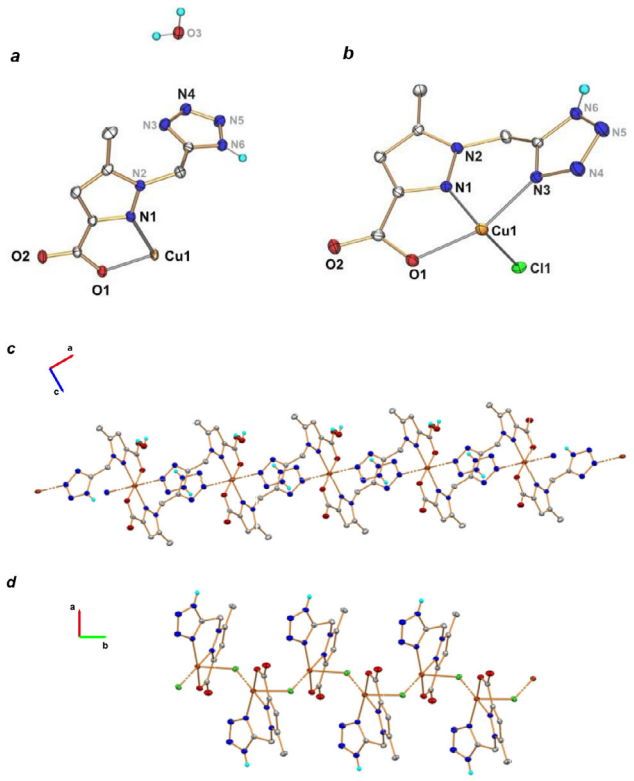


**FIGURE 6** | Asymmetric unit of the coordination polymer: (**a**) {[Cu(**HL$_4$**')]·$H_2O$}$_n$ (**10**); (**b**) [Cu(**HL4**')Cl]$_n$ (**11**). (**c**) 1D polymeric chain of {[Cu(**HL4**')]·$H_2O$}$_n$, with Cu(II) centers bridged by **HL4**' ligands, propagating along the *a* axis. Water molecules of crystallization are also depicted; (**d**) 1D polymeric chain of [Cu(**HL4**')Cl]$_n$, with Cu(II) centers bridged by chloride ions ($Cl^-$), propagating along the *b* axis.

at the inversion center in a distorted [$CuN_4O_2$] octahedral coordination geometry with the $\Sigma$ parameter being 51.5°, with one crystallization water molecule associated with each copper center. Two bidentate **HL$_4$**' ligands (**HL$_4$** after hydrolysis) occupy the equatorial positions, with each ligand coordinating to $Cu^{II}$ through one nitrogen atom (N(1)$_{pz}$) and one oxygen atom (O(1)), forming a five-membered chelate ring. The "bite" angle of the ligand, ∠N(1)–Cu(1)–O(1), is 81.57(5)° (Table S14). The Cu(1)–N(1)$_{pz}$ and Cu(1)–N(4)$_{ttrz}$ bond lengths are 1.9838(13) and 2.573 Å, respectively. The apical positions are occupied by two nitrogen atoms (N(4)$_{ttrz}$), each from the tetrazole group of a different **HL$_4$**' ligand. **HL$_4$**' ligands bridge the $Cu^{II}$ centers with the Cu(1)···Cu(1) distance of 7.334 Å, leading to the formation of a 1D neutral looped chain along the crystallographic *a* axis (Figure S6). The dihedral angle between the planes of a pyrazole and a tetrazole ring is 82.80°.

The coordination polymer [Cu(**HL4**')Cl]$_n$ (**11**) forms crystals in the monoclinic crystal system, with the space group $P2_1/c$. The asymmetric unit consists of one $Cu^{II}$ ion, a tridentate ligand, and one $Cl^-$ ion (Figure S6). The $Cu^{II}$ ion is in a distorted square-pyramidal geometry being coordinated with two nitrogen atoms and one oxygen atom from the ligand and two bridging chloride ions. The Addison distortion parameter $\tau_5$ is 0.17°, indicating a geometry closer to square-pyramidal (SPY). The bite angles of the six- and five-membered chelate rings are 86.45(6)° and 79.48(5)° for ∠N(1)$_{pz}$—Cu(1)—N(3)$_{ttrz}$ and ∠N(1)$_{pz}$—Cu(1)—O(1), respectively (Table S15). The Cu(1)—N(1)$_{pz}$ and Cu(1)—N(3)$_{ttrz}$ bond lengths are 1.9428(13) and 2.0118(13) Å, respectively. They are comparable to the reported $Cu^{II}$ complexes containing azole type ligands [52–56]. The equatorial Cu(1)—Cl(1) distance is 2.2117(4) Å, which is shorter than the apical Cu(1)—Cl(1) bond length [2.7035(5)Å]. The latter is attributed to the Jahn–Teller effect of the $d^9$ electron configuration [57]. Cl(1) atom bridges between adjacent $Cu^{II}$ ions to form the right handed helical chain. The Cu(1)···Cu(1) distance in the chain is 4.615 Å, which is longer than in the similar compounds with dichloro-bridging [58] and single chloro-bridging [59]. The dihedral angle between the planes of pyrazole and tetrazole ring is 33.30°.

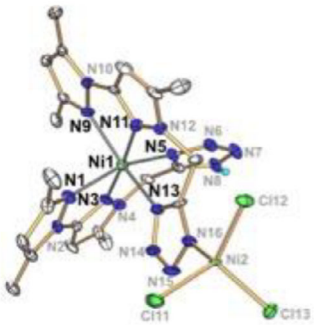


**FIGURE 7** | Molecular structure of dinuclear Ni(II) complex (**14**).

## 2.8 | $Ni^{II}$ Dinuclear Complex 14

Complex **14** crystallizes in the triclinic system, space group *P* –1. Two ligands **HL6** are coordinated to a central $Ni^{II}$ ion in a tridentate manner, with one ligand in its deprotonated form bridging the Ni(**HL6**) unit and the $Ni^{II}$ atom coordinated to three chloride ions. This results in the formation of a dinuclear $Ni^{II}$ complex (Figure 7), with the distance between the two nickel centers measured at 6.160 Å. Bond valence analysis and the overall charge balance indicate $Ni^{II}$ ions. The coordination environment around the nickel centers is however distinctive. The central $Ni^{II}$ ion (Ni(1)) adopts a distorted octahedral geometry, with a distortion parameter Σ of 95.2°, indicating a slight deviation from ideal octahedral geometry. The second $Ni^{II}$ ion (Ni(2)) adopts a near-perfect tetrahedral configuration ($\tau_4$ = 0.92).

The bond lengths between the nickel center (Ni(1)) and the nitrogen atoms in the ligands exhibit notable variation. The Ni(1)—N$_{pz}$ bond lengths differ, with those *trans* to a pyrazole nitrogen being shorter, averaging 2.024(8) Å, in contrast to those *trans* to a tetrazole nitrogen, which average 2.141(8) Å. The average Ni(1)—N$_{ttrz}$ bond length is 2.081(8) Å. Additionally, the Ni(2A)—Cl bond length is 2.244(3) Å, while the Ni(2)—N$_{ttrz}$ bond length is 2.078(9) Å. (Table S16). Two dinuclear $Ni^{II}$ complexes interact with one another *via* hydrogen bonds involving the tetrazole groups and water molecules, resulting in the formation of tetramers (Figure 7).

## 2.9 | Hirshfeld Surface Analysis

Complementary to the single crystal X-ray diffraction, the Hirshfeld surface analysis was used to gain deeper insights into

nature, strength and the extent of intermolecular interactions governing crystal packing, as well as to provide a comparison between the metal complexes presented herein. The Hirshfeld surface and 2D fingerprint calculations were performed using CrystalExplorer version 21.5 [60] on crystal structures imported from the corresponding CIF files. Disordered structures were treated by manually editing CIF to choose one of the disordered components, thereby implying full occupancy of all atoms used for the surface generation. In case of cationic complexes, noncoordinating anion was not taken into consideration for the calculation of the Hirshfeld surface and generation of the 2D fingerprint plot. For coordination polymers **5**, **7**, **10,** and **11**, HS and FPs were generated taking the entire polymer chain into consideration. In all cases, surface transparency was enabled in order to enhance the visualisation of the short contacts.

Following the Hirshfeld partitioning scheme proposed by Spackman and Byrom [61], the electron density of the crystal is divided into molecular fragments. With the distance between each point on the Hirshfeld surface and the atoms on the inside or the outside of the surface defined as $d_i$ and $d_e$, respectively, a color-coded map can be generated. Thus, the interatomic interactions within the crystal can be quantified effectively, where visual representation is achieved through the presence of red spots, highlighting interatomic contacts shorter than the sum of the corresponding van der Waals radii, thus indicating potential hydrogen bonds.

Further characterization of the interatomic contacts in the crystal structure can be achieved by examining Fingerprint plots (FP) including both $d_i$ and $d_e$.

The Hirshfeld surfaces of complexes **1–11** and **14** are shown in Figures 8 and 9 and display surfaces mapped over the range −0.5 to 1.5 Å for $d_{norm}$, −1.0 to 1.0 Å for shape index, and −4.0 to 0.4 Å for curvedness. Figure 10

Mononuclear metal complexes bearing ligand **L1** exhibited very similar intermolecular interactions as a result of the crystal packing. Interactions within the crystal structures of **1**, **2**, **3,** and **4** with the adjacent molecule are dominated through C–H···O hydrogen bonding (O···H/H···O = 18.4% for **1**, 19.2% for **2**, 22.2% for **3**, and 24.3% for **4**) with the perchlorate (**1**, **2**, **3**) and the nitrate anions or the solvent molecules (**4**), as well as van der Waals contacts involving $CH_2$ and $CH_3$ groups of the ligand and the nitrogen atoms of the nitrile, pyrazole and triazole moieties (N···H/H···N = 22.6% for **1**, 24.8% for **2**, 24.2% for **3**, and 20.5%).

Hydrogen bonding can be identified in the corresponding 2D Fingerprint plots of **1**, **2, 3,** and **4** as sharp spikes at shorter $d_i$ and $d_e$ distances (Figures S44–47) and through the presence of red spots in the Hirshfeld surface, whereas the van der Waals interactions are indicated through blue and white areas with faint red spots (Figure 8).

While the O···H/H···O 2D FPs of **1**, **2,** and **3** show an asymmetric area in respect to the diagonal $d_i = d_e$ due to the oxygen atoms occupying outside of the Hirshfeld surface, 2D FP of **4** is symmetrical.The N···H/H···N 2D FPs of all four complexes are symmetric involving slightly sharper spikes implying more directional weak hydrogen bonding and large diffuse areas related

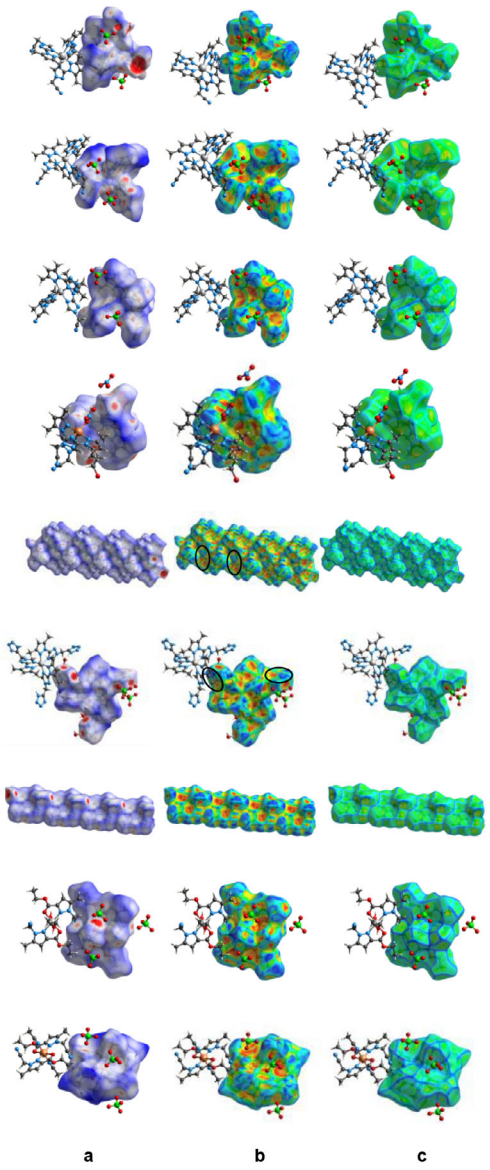


**FIGURE 8** | View of the Hirshfeld surface of complexes **1–9** plotted over $d_{norm}$ (**a**), shape index (**b**) and curvedness (**c**). The adjacent red and blue triangles that reveal $\pi\cdots\pi$ stacking interactions are highlighted by black circles.

to the van der Waals interactions. Significant proportion of the interactions contributing to packing in the crystal structure of **1–4** are the H···H contacts comprising 31.9%, 30.7%, 31.5%, and 27.4% of the Hirshfeld surface, respectively. Anion···$\pi$ interactions can also be detected in the proximity of the perchlorate anion to the pyrazole ring (C···O/O···C = 2.4% (**1**), 4.2% (**2**), 2.4% (**3**), 2.0% (**4**); C···H/H···C = 10.7% (**1**), 10.2% (**2**), 9.8% (**3**), 11.1% (**4**)). In **6**, presence of the tetrazole moiety in the ligand **HL2** and water molecules in the lattice result in hydrogen bonding interactions O—H···N and N—H···O (N···H/H···N = 27.5% and O···H/H···O = 22.3%) between the proton and the oxygen of the water molecule and the nitrogen and the proton of the tetrazole ring, respectively. They are also estimated to be stronger compared to those of **1–4** and **8–9**. This is evident in the two sharp spikes in the 2D FP at $d_i+d_e$ = 1.7 Å for O···H and $d_i+d_e$ = 1.8 Å for N···H hydrogen bonding (Figure S49) as well as

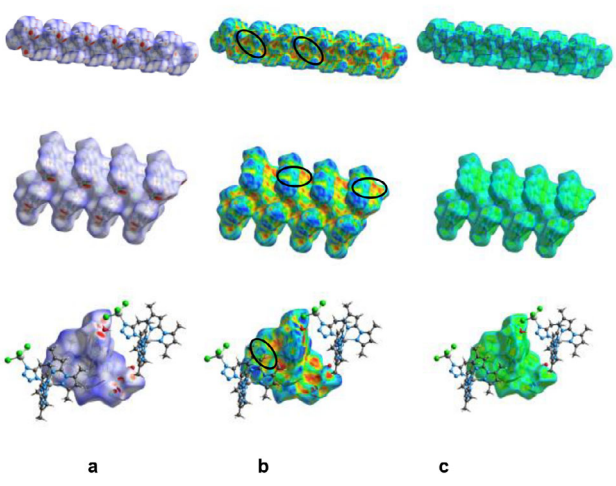


**FIGURE 9** | View of the Hirshfeld surface of complexes **10**, **11** and **14** plotted over $d_{norm}$ (**a**), shape index (**b**) and curvedness (**c**). The adjacent red and blue triangles that reveal $\pi\cdots\pi$ stacking interactions are highlighted by black circles.

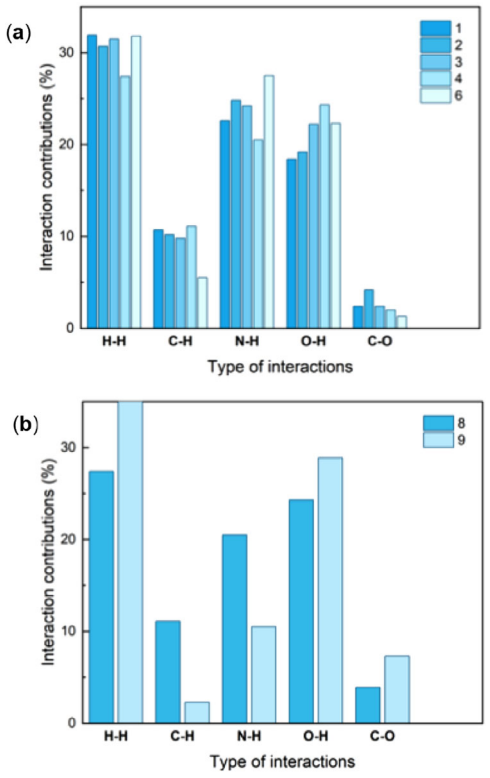


**FIGURE 10** | Percentage contributions of various interactions to the Hirshfeld surface for complexes **1–4, 6** (**a**) and **8**, **9** (**b**).

large red spots on the $d_{norm}$ Hirshfeld surface (Figure 8). Weaker C—H···O hydrogen bonding with the perchlorate anions and the anion···$\pi$ interactions between the perchlorate oxygen and the triazole ring are present as well, albeit to a lesser extent compared to **1–3** (C···O/O···C = 1.3%, C···H/H···C = 5.5%). As in previous complexes, H···H contacts are most dominant (H···H = 31.8%) denoted by blue and white areas on the Hirshfeld surface. $\pi\cdots\pi$ stacking interactions between the tetrazole and triazole rings of the adjacent molecules in- and outside of the surface are highlighted by characteristic alternating blue and red triangles in the shape index functions and flat green area separated by sharp blue edges in the curvedness function.

Molecules of methanol coordinated to the cobalt metal centre contribute to a high degree of hydrogen bonding in the crystal of **8**, compared to **9**, which is obvious from the absence of characteristic sharp spikes in the 2D FP (Figure S51,S52). In **8**, O—H···O interactions with the perchlorate anion show on the Hirshfeld surface as large red spots and characteristic sharp spikes in the 2D FP (O···H/H···O = 32.8%) at $d_i+d_e$ = 1.8 Å (Figure S51). In contrast, 2D FP of **9** shows a single small spike at $d_i+d_e$ = 2.2 Å from weak C—H ···O interactions between protons of the **L3** ligand and the perchlorate anion outside of the Hirshfeld surface (O···H/H···O = 28.9%). Complexes **8** and **9** display somewhat weaker C—H ···O and C—H ···N hydrogen bonding interactions involving protons of the **L3** ligand and the perchlorate anion and the nitrile nitrogen, respectively (N···H/H···N = 12.7%, $d_i+d_e$ = 2.3 Å (**8**) and N···H/H···N = 10.5%, $d_i+d_e$ = 2.6 Å (**9**)).

In **14**, the 2D FP contains a sharp spike implying strong N—H···O hydrogen bonding interaction between the tetrazole hydrogen and the water molecules present in the crystal lattice (large red spots on the $d_{norm}$ Hirshfeld surface) (Figures S55 and 9). It accounts for only 1.6% of the Hirshfeld surface, in contrast to the previously analysed mononuclear complexes. Other hydrogen bonding interactions include O—H···N of the lattice water and the tetrazole nitrogen (N···H/H···N = 21.1%), as well as C—H···Cl contacts (Cl···H/H···Cl = 25.5%) between the chlorido ligands and the methyl groups on the pyrazole ring of **HL6** (Figure S55). Similarly to the complexes discussed previously, H···H van der Waals contacts dominate the Hirshfeld surface and contribute to the efficient crystal packing (H···H = 32.7%). Moreover, shape index and curvedness functions indicate a degree of $\pi\cdots\pi$ stacking interactions between pyrazole rings of the adjacent molecules. Overall, the mononuclear complexes **1–4**, **8,** and **9**, which were investigated for their cytotoxicity do not seem to exhibit significant differences in the interactions mainly contributing to their crystal packing. Therefore, it is reasonable to assume that any major differences in their biological activity can be attributed to the activity of the metal centre, as well as possible ligand dissociation in solution (e.g. labile apical ligands in **8** and **9**). It is, however, notable that the complexes **6** and **8** exhibit the strongest hydrogen bonding interactions (O···H and N···H in **6** and O···H in **8**) in the series.

A prominent feature of the corresponding 2D FP plot of **5** is a very sharp spike attributed to C···C interactions (Figure S48), which stems from the parallel $\pi\cdots\pi$ stacking interaction of the pyrazole and triazole rings of the ligand (C···C = 2.3%, C···N/N···C = 4.7%). Coordination polymers **5**, **10,** and **11** share the feature of parallel (**5**) and antiparallel (**10**, **11**) $\pi\cdots\pi$ stacking interactions that contribute to the efficient packing in the crystal lattice. This is characterised by motifs of alternating blue and red triangles on the Hirshfeld surface with the shape index function.

A characteristic of the Hirshfeld surface of **5** and **7** is a series of red spots along the polymer chain that highlight the C–H···Cl hyrogen bonding interaction between the bridging chlorido ligands and the protons of **L1,** and the chlorido ligands and the protons of the triazole rings and the $CH_2$ groups (Cl···H/H···Cl = 19.9% (**5**),

30.2% (**7**)). N···H contacts are mostly van der Waals interactions, which can be deduced from the absence of characteristic red spots on the Hirshfeld surface (N···H/H···N = 24.1% (**5**), 20.9% (**7**)). Other notable van der Waals contacts responsible for the crystal packing of **5** and **7** are H···H contacts (30.1% (**5**), 24.1% (**7**)). On the other hand, due to the presence of a water molecule in the asymmetric unit of **10**, O—H···O hydrogen bonding interactions are dominating the 2D FP of the Hirshfeld surface

(O···H/H···O = 24.6%) as two distinct spikes at $d_i+d_e$ = 1.6 Å indicating a strong interaction (Figure S53). This is also shown in Figure 9 of the $d_{norm}$ Hirshfeld surface of **10** as large red spots, which highlight the interaction between the water molecules in- and outside of the Hirshfeld surface with the carbonyl oxygens of **HL4'** of the polymer chain, as well as the tetrazole protons and the oxygen atoms of the lattice water.

Similarly to **5** and **7**, N···H interactions (N···H/H···N = 23.3%) mainly comprise of van der Waals contacts. However, a small contribution of C—H···N hydrogen bonding cannot be excluded, based on relatively indistinct spikes in the 2D FP with isolated N···H/H···N contacts. An important contribution to the crystal packing of **10** comes from H···H contacts forming a characteristic small spike in the 2D FP (H···H = 29.7%).

An interesting hallmark of the crystal packing of **11** is the presence of Cu···H, Cu···C and Cu···Cl contacts (Cu···H/H···Cu = 1.3%, Cu···C/C···Cu = 1.7%, Cu···Cl/Cl···Cu = 0.8%) that contribute to stabilising the crystal packing, not observed in the previously discussed coordination compounds. Large red spots on the Hirshfeld surface with the $d_{norm}$ function indicate presence of strong hydrogen bonding interactions. This results in two sharp spikes on both sides of the $d_i = d_e$ diagonal in the 2D FP ($d_i+d_e$ = 1.7 Å), and involves the carbonyl oxygen atoms and the tetrazole protons of **HL4'** of the two adjacent polymer chains (Figure S54). Cl···H contacts are observed as weak red spots on the Hirshfeld surface between bridging chlorido ligands and the protons of the pyrazole ring and as slight spikes in the 2D FP at $d_i+d_e$ = 2.7 Å (Cl···H/H···Cl = 12.1%). N···H interactions are largely van der Waals interactions (N···H/H···N = 22.7%), as indicated by white areas above the tetrazole rings, denoting their interaction with the $CH_2$ groups of **HL4'**. Interactions of the perpendicularly positioned tetrazole rings of the adjacent polymer chains involve other van der Waals contacts (C···N/N···C = 6.5%, N···N = 3.2%).

## 2.10 | Cytotoxicity in human Cancer Cell Lines

MTT assays were performed in three human tumor cell lines (A549 lung adenocarcinoma, CH1/PA-1 ovarian teratocarcinoma, and SW480 colon carcinoma cells) for 72 h (for concentration–effect curves see Figures S56 and S57). $IC_{50}$ values (Table 2) indicate inactivity of **L1**, **L3** and **L5** in all three cell lines, but a certain activity of complexes **2–4** and **8**, **9**, **12** and **13**, depending on the cell line, with Co complexes **2** and **8** being the most potent in CH1/PA-1 (~50 μM) and SW480 cells (~15 μM).

Differences in sensitivity between the cell lines, especially between the broadly chemosensitive CH1/PA-1 and the multidrug-resistant A549 cells (which are also the least sensitive to many of the compounds tested here) are mostly moderate.

**TABLE 2** | Cytotoxic potency (mean $IC_{50}$ values ± standard deviations, $n \geq 3$, in μM) of tested compounds (including corresponding simple metal salts and platinum drugs as reference compounds) in three human cancer cell lines, determined by means of 72-h MTT assays (~ 200 μM indicates that an $IC_{50}$ value was not reached in each of the experiments).

| Compound | A549 | CH1/PA-1 | SW480 |
|---|---|---|---|
| **L1** | > 200 | > 200 | > 200 |
| **L3** | > 200 | > 200 | > 200 |
| **L5** | > 200 | > 200 | > 200 |
| **1** | ~ 200 | > 200 | > 200 |
| **2** | ~ 200 | 47 ± 17 | 15 ± 9 |
| **3** | 171 ± 23 | 91 ± 12 | ~ 200 |
| **4** | 127 ± 16 | 101 ± 12 | ~ 200 |
| **8** | > 200 | 66 ± 9 | 14 ± 6 |
| **9** | ~ 200 | 104 ± 24 | > 200 |
| **12** | 143 ± 3 | 91 ± 9 | 168 ± 23 |
| **13** | ~ 200 | 106 ± 27 | > 200 |
| **$FeSO_4$** | > 200 | > 200 | > 200 |
| **$NiCl_2$** | > 200 | 97 ± 16 | > 200 |
| **$CoCl_2$** | 169 ± 27 | 85 ± 20 | 9.2 ± 2.6 |
| **$CuCl_2$** | 153 ± 10 | 110 ± 14 | > 200 |
| **Cisplatin** | 5.3 ± 1.8 | 0.10 ± 0.02 | 3.1 ± 0.5 |
| **Oxaliplatin** | 3.0 ± 1.7 | 0.14 ± 0.01 | 0.39 ± 0.16 |

Only for complexes **2** and **8**, $IC_{50}$ values differ by more than a factor of two between these cell lines. The consistent sensitivity of SW480 cells to $Co^{II}$ compounds (**2**, **8** and $CoCl_2$) is remarkable since nearly none of the other compounds yielded an $IC_{50}$ value in the tested range of up to 200 μM in this cell line and since this exclusive sensitivity is not paralleled in A549 cells. Comparison of the $Fe^{II}$, $Co^{II}$, $Ni^{II}$ , and $Cu^{II}$ complexes (**1**–**4**) with the same ligand **L1** indicates distinct differences: In the CH1/PA-1 cell line, the iron complex is completely inactive and the cytotoxic potency of the other complexes increases in the order $Cu^{II} \leq Ni^{II} < Co^{II}$. (The inactivity of $Fe^{II}$ complex **1** also implies that any cytotoxicity that might arise from perchlorate is negligible here.) Whereas the complexes are at least more cytotoxic than the inactive ligands in the majority of cases, comparison with corresponding simple salts (cf. **1** with $FeSO_4$; **3**, **12** and **13** with $NiCl_2$; **2** and **8** with $CoCl_2$; **4** and **9** with $CuCl_2$) reveals no consistent superiority for any of these complexes. Nevertheless, the specific sensitivity of SW480 colon cancer cells to $CoCl_2$ and its metal complexes stands out as a finding that might deserve further attention.

As mentioned above, complex **8**, $[Co(MeOH)_2(\mathbf{L3})_2](ClO_4)_2$, is a dicationic $Co^{II}$ species with a distorted-octahedral coordination environment in which two **L3** ligands bind N,O-chelate in the equatorial plane ($\Sigma$ = 64.1°, ∠N—Co—O = 76.5°) and two MeOH molecules occupy the axial positions. In cytotoxicity assays, **8** displays pronounced activity in SW480 cells ($IC_{50}$ = 14 ± 6 μM), while the free ligand **L3** is inactive (>200 μM). Its potency profile parallels that of $CoCl_2$, suggesting that cobalt is the main effector and that the ligand environment does not confer

a fundamentally different mode of action. Given the presence of axial solvent donors, formation of aqua/solvent variants in biological media is plausible and could facilitate engagement with cellular targets; however, consistent with our data, we refrain from assigning a specific pathway. We therefore interpret **8** as a ligand-modulated cobalt delivery scaffold whose activity aligns with cobalt's intrinsic profile.

## 3 | Conclusions

In this study, we successfully synthesized and thoroughly characterized a series of novel tetrazole-triazole-pyrazole and tetrazole-pyrazole ligands, along with their corresponding coordination complexes and coordination polymers. Detailed spectroscopic analyses, including single-crystal X-ray diffraction, revealed the diversity and versatility of their molecular and crystal structures.

The cytotoxic activity of these newly developed coordination compounds was evaluated against three cancer cell lines: A549, CH1/PA-1, and SW480, all of which represent clinically relevant cancer types. While the free ligands displayed limited cytotoxicity ($IC_{50}$> 200 μM), several of their metal complexes showed significantly enhanced performance. Notably, complexes **2** and **8** demonstrated remarkable potency against SW480 cells, with $IC_{50}$ values of about 15 μM, indicating distinct activity even at low concentrations. These two compounds also performed well against CH1/PA-1 cells, achieving $IC_{50}$ values of 47 and 66 μM, respectively. In contrast, activity against the A549 cell line was less pronounced.

This work underscores the potential of hybrid systems combining organic scaffolds and transition metals to yield to biologically active coordination compounds with promising anticancer properties. These findings contribute meaningfully to the growing field of metal-based therapeutics and open perspectives for the design of new and more performer agents. Future studies should focus on elucidating the mechanisms of action, selectivity, and evaluating in vivo efficacy and safety, as well as exploring structural modifications to further enhance their biological activity.

## 4 | Experimental Section

### 4.1 | Materials and Instrumentation

All chemicals were purchased and used as received without further purification unless otherwise stated.

Nuclear magnetic resonance ($^1$H and $^{13}$C NMR) spectra of ligands **L1**, **HL2**, **L3,** and **HL4** (Figures S17–S24) were recorded at ambient temperature using a Bruker Avance II 300 MHz instrument. Chemical shifts ($\delta$) are reported in parts per million relative to residual DMSO-$d_6$ ($\delta$ = 2.50 ppm for $^1$H and 39.5 ppm for $^{13}$C). Coupling constants are expressed in Hertz (Hz). The following abbreviations are used: *s* = singlet, *d* = doublet, *t* = triplet, *q* = quartet. High-resolution electrospray ionization mass spectra (HR-ESI-MS) of ligands **L1**, **HL2**, **L3,** and **HL4** and complexes **1–4** and **8** (Figures S25–32 and S36) were recorded using a ThermoFisher Q-Exactive. High-resolution electrospray ionization mass spectra (HR-ESI-MS) of complexes **5–7** and **9–14** (Figures S33–35 and S37–S41) were recorded on a *maXis* QTOF-MS instrument (*Bruker Daltonics* GmbH, Bremen, Germany).

Melting points were measured using a Koffler bench.

Elemental analyses were performed on an EA 3000 CHNS-O Elemental Analyser from EuroVector at the Laboratory for Microanalytical Services of the University of Vienna.

Powder X-ray diffraction (PXRD) patterns were collected on a D8-Advance diffractometer (Bruker, Germany) with Cu$K_\alpha$ radiation ($\lambda$ = 1.5148 Å) operating at 40 kV and 30 mA.

Fourier transform infrared (FT-IR) spectroscopy measurements were performed using an Equinox 55 (Bruker) equipped with an ATR module and an MCT detector. The Bruker OPUS software was used for data processing (including ATR correction). The letters *s*, *i*, *m* and *w* correspond to strong, intense, medium and weak peaks respectively.

UV-visible spectroscopy measurements were performed using a Shimadzu 3600 plus spectrometer equipped with Harrick's Praying Mantis, which allows direct analysis of powders in reflectance mode.

Mössbauer measurements were performed in transmission geometry with a constant acceleration mode conventional spectrometer equipped with a 50 mCi $^{57}$Co(Rh) source and a Reuter Stokes proportional counter. The powdered sample was sealed in plastic sample holder and the spectrum was fitted with Recoil 1.05 Mössbauer Analysis software [62]. Isomer shift is given relative to $\alpha$-Fe at ambient temperature.

Magnetic susceptibilities measurements were performed on a Quantum design MPMS-5s SQUID magnetometer. Magnetic data were corrected for the sample holder and diamagnetic contributions.

### 4.2 | X-Ray Crystallography

Single crystals suitable for X-ray measurements were selected and mounted onto a rubber loop using Fomblin oil.

X-ray diffraction data for complexes **1**, **2**, **8**, and **9** were recorded at ambient temperature on an MAR345 image plate using Mo$K_\alpha$ radiation ($\lambda$ = 0.71073 Å) generated by an Incoatec microfocus source (Montel optics). Data integration and reduction were performed using CrysAlis$^{PRO}$ software, and absorption correction was applied [63]. The structure was solved by SHELXT [64] and refined using least-squares against $F^2$ in SHELXL2018/3 [65]. For complex **1**, both $ClO_4^-$ anions were disordered over two sites, and similarity restraints were applied to restrain their geometry, with isotropic restraints on the oxygen atoms and rigid bond restraints for thermal ellipsoid control. Two terminal C≡N groups were also disordered but refined without additional restraints. For complex **2**, the single crystal was coated with varnish to protect it and slow down solvent evaporation. The structure contained solvent cavities (9.9% of the unit cell volume) over two identical sites, and diffuse solvent was handled using the

SQUEEZE algorithm in Platon [66]. Both $ClO_4^-$ anions were disordered, with one modeled over two sites and the other over three. Similarity restraints were set up to restrain the geometry of the disordered $ClO_4^-$ anions with isotropic restraints used to control their thermal ellipsoids.

Single-crystal X-ray diffraction data for complexes **3**, **4**, **5**, **6**, **10,** and **11** were collected at 150 K using an Xcalibur Oxford diffractometer with a Sapphire 3 CCD detector and a 4-cycle Kappa geometry goniometer. $MoK_\alpha$ radiation ($\lambda$ = 0.71073 Å) was used. Data collection, reduction, and cell refinement were performed with CrysAlis CCD and CrysAlis RED software. Structure solution and refinement were done using SHELXS-2014 [67] and SHELXL-2014 [68] within the WinGX package [69], with empirical absorption corrections applied [70].

X-ray diffraction data for complex **7** were collected on a Rigaku R-AXIS RAPID II diffractometer using $MoK_\alpha$ radiation ($\lambda$ = 0.71075 Å). The structure was solved by direct methods [71] and refined by full-matrix least-squares techniques using the SHELXL [70] and Crystal Structure [72] packages. Non-hydrogen atoms were refined anisotropically, and solvent molecule sites were identified and included in the refinement.

Single-crystal X-ray diffraction data for complex **14** were collected on a STOE StadiVari Eulerian 4-circle diffractometer, equipped with a multilayer monochromator, Mo $K_\alpha$ INCOATEC microfocus sealed tube, and Oxford cooling system. The crystal structure was solved by direct methods, with non-hydrogen atoms refined anisotropically and hydrogen atoms placed at calculated positions and refined with a riding model. OLEX2 [73] for structure solution, refinement, molecular diagrams, and graphical user-interface, ShelXle [74] for refinement and graphical user-interface, SHELXS-2015 [76] 5or structure solution, SHELXL-2015 [76] for refinement, and Platon [77] for symmetry check were used.

Final unit cell data and refinement statistics for compounds **1–11** and **14** are collated in Table S2. 'DepositionNumber(s) "https://www.ccdc.cam.ac.uk/services/structures?id = https://doi.org/10.1002/chem.202502238">2266412-2266418 (for **1–7**), 2408280 (for **8**), 2408282 (for **9**), 2408281 (for **10**), 2408283 (for **11**) and 2400722 (for **14**) </url> contain(s) the supplementary crystallographic data for this paper. These data are provided free of charge by the joint Cambridge Crystallographic Data Centre and Fach informations zentrum Karlsruhe <url href = "http://www.ccdc.cam.ac.uk/structures">Access Structures service.'

## 4.3 | Synthesis Section

Starting materials: 3-(3,5-dimethyl-1*H*-pyrazol-1-yl)-1*H*-1,2,4-triazole (**A1**) and ethyl 5-methyl-1*H*-pyrazole-3-carboxylate (**A2**) as well as ligands: 2-(3,5'5'-trimethyl'1'H-[1'3'-bipyrazol]'1'-yl)acetonitrile (**L5**) and 1'-((1H-tetrazol-5-yl)methyl)-3,5'5'-

trimethyl'1'H-1'3'-bipyrazole (**HL6**) were prepared according to the recently reported procedures [78, 79]. (**Scheme 1**).

### 4.3.1 | Synthesis of 2-(3-(3,5-dimethyl-1*H*-pyrazol-1-yl)-1H-1,2,4-triazol-1-yl)Acetonitrile (L1)

2-chloroacetonitrile (2.54 g, 33.7 mmol, 1.1 eq.) was slowly added to a mixture of 3-(3,5-dimethyl-1*H*-pyrazol-1-yl)-1*H*-1,2,4-triazole (**A1**) (4.99 g, 30.6 mmol, 1 eq.) and *t*-BuOK (5.15 g, 45.9 mmol, 1.5 eq.) in THF (50 mL) and the mixture was refluxed for 1 h. After cooling to 0°C, the reaction mixture was refluxed for an additional 3 h. The mixture was then filtered, washed with THF (10 mL), and concentrated under reduced pressure. The resulting residue was purified by column chromatography on silica gel, using a hexane/ethyl acetate (2:8) eluent. The desired product was precipitated by the addition of diethyl ether (7 mL). Yield: 52% (3.28 g). M. p.: 112°C. $R_f$ = 0.48. $^1$H NMR (300 MHz, DMSO-$d_6$, $\delta$ (ppm)): 8.68 (s, 1H, $\boldsymbol{H}_{(trz)}$), 6.10 (m, 1H, $\boldsymbol{H}_{(pz)}$), 5.63 (s, 2H, C$\boldsymbol{H}_2$-CN), 2.41 (s, 3H, C$\boldsymbol{H}_3$), 2.17 (s, 3H, C$\boldsymbol{H}_3$). $^{13}$C NMR (75 MHz, DMSO-$d_6$, $\delta$ (ppm)): 157.8 (1C, $\boldsymbol{C}_{(trz)}$-pz), 149.5 (1C, $\boldsymbol{C}_{(pz)}$-$CH_3$), 145.7 (1C, $\boldsymbol{C}$ = $N_{(trz)}$), 141.1 (1C, $\boldsymbol{C}_{(pz)}$-$CH_3$), 115.1 (1C, $\boldsymbol{C}$≡N), 107.9 (1C, $\boldsymbol{C}$ = $C_{(pz)}$), 37.5 (1C, $\boldsymbol{C}H_2$-CN), 13.3 (1C, $\boldsymbol{C}H_3$), 12.3 (1C, $\boldsymbol{C}H_3$). FT-IR (KBr, $cm^{-1}$): 3097 (w), 2920 (w), 2351 (w), 1549 (i), 1554 (i). ESI-MS (+): *m/z* found = 203.10409, *m/z* calcd for [(**L1**)+H]$^+$: 203.10397. Anal. Calcd for $C_9H_{10}N$ (**L1**): C, 53.46; H, 4.98; N, 41.56. Found: C, 53.30; H, 4.91; N, 40.84.

### 4.3.2 | Synthesis of 5-((3-(3,5-dimethyl-1H-pyrazol-1-yl)-1H-1,2,4-triazol-1-yl)Methyl)-1H-tetrazole (HL2)

A suspension of sodium azide (0.47 g, 7.3 mmol, 1 eq.), zinc chloride (1.0 g, 7.4 mmol, 1.5 eq.), and **L1** (1.0 g, 5 mmol, 1 eq.) in water (80 mL) was refluxed for 12 h. After the mixture was cooled to ambient temperature, concentrated HCl (2 mL) was added, and the white precipitate of desired product was filtered off. Yield: 53% (0.8 g). M. p. > 260°C. $^1$H NMR (300 MHz, DMSO-$d_6$, $\delta$ (ppm)): 8.75 (s, 1H, $\boldsymbol{H}_{(trz)}$), 6.10 (s, 1H, $\boldsymbol{H}_{(pz)}$), 5.76 (s, 2H, C$\boldsymbol{H}_2$), 2.37 (s, 3H, C$\boldsymbol{H}_3$), 2.14 (s, 3H, C$\boldsymbol{H}_3$). $^{13}$C NMR (75 MHz, DMSO-$d_6$, $\delta$ (ppm)): 156.7 (1C, $\boldsymbol{C}_{(ttrz)}$), 156.3 (1C, $\boldsymbol{C}_{(trz)}$-pz), 149.7 (1C, $\boldsymbol{C}_{(pz)}$-$CH_3$), 145.0 (1C, $\boldsymbol{C}$ = $N_{(trz)}$), 141.0 (1C, $\boldsymbol{C}_{(pz)}$-$CH_3$), 108.2 (1C, $\boldsymbol{C}$ = $C_{(pz)}$), 44.5, (1C, $\boldsymbol{C}H_2$-ttrz), 13.1 (1C, $\boldsymbol{C}H_3$), 12.2 (1C, $\boldsymbol{C}H_3$). FT-IR (KBr, $cm^{-1}$): 3117 (w), 2351 (m), 1599 (i), 1517 (m). ESI-MS (+): *m/z* found = 246.1210, *m/z* calcd for [(**HL2**)+H]$^+$: 246.12102.

### 4.3.3 | Synthesis of Ethyl 1-(cyanomethyl)-3-methyl-1*H*-pyrazole-5-carboxylate (L3)

To a solution of ethyl 5-methyl-1*H*-pyrazole-3-carboxylate (**A2**) (0.49 g, 3.2 mmol) in diethyl ether (30 mL), *t*-BuOK (0.54 g, 4.8 mmol) was added, and the mixture was heated to reflux for 1 h. After cooling to 0°C, 2-chloroacetonitrile (0.25 mL, 3.4 mmol) was added dropwise. The reaction mixture was then refluxed for 3 days, followed by filtration. The solvent was evaporated under reduced pressure and the residue was purified by column chromatography (silica gel, $CH_2Cl_2$/Hexane: 2/8) to yield the product (**L3**) as a solid. Yield: 40% (0.2 g). M. p.: 78°C. $R_f$ = 0.7 (Ethyl acetate). $^1$H NMR (300 MHz, DMSO-$d_6$, $\delta$ (ppm)): 6.62 (*d*, *J* = 0.8 Hz, 1H, $H_{(pz)}$), 5.56 (*s*, 2H, C$\boldsymbol{H}_2$-CN), 4.26 (*q*, *J* = 7.1 Hz, 2H, C$\boldsymbol{H}_2$-$CH_3$), 2.35 (*d*, *J* = 0.7 Hz, 3H, C$\boldsymbol{H}_3$), 1.28 (*t*, 3H, $CH_2$-C$\boldsymbol{H}_3$).

$^{13}$C NMR (75 MHz, DMSO-$d_6$, $\delta$ (ppm)): 161.4 (1C, ***C*** = O), 142.45 (1C, ***C*** = $N_{(pz)}$), 142.09 (1C, $\boldsymbol{C}_{(pz)\text{-}}CH_3$), 115.94 (1C, ***C***≡N), 109.13 (1C, ***C*** = $C_{(pz)}$), 60.94 (1C, $\boldsymbol{C}H_{2\text{-}}O$), 38.21 (1C, $\boldsymbol{C}H_{2\text{-}}CN$), 14.77 (1C, $CH_{2\text{-}}\boldsymbol{C}H_3$), 10.98 (1C, $\boldsymbol{C}H_{3(pz)}$). FT-IR (KBr, cm$^{-1}$): 2962 (w), 2112 (w), 1762 (i), 1456 (w), 1056 (w). ESI-MS (+): *m/z* found = 194.09259, *m/z* calcd for [(**L3**)+H]$^+$: 194.09240. Anal. Calcd for $C_9H_{11}N_3O_2$ (**L3**): C, 55.95; H, 5.74; N, 21.75. Found: C, 55.93; H, 5.76; N, 21.39.

#### 4.3.4 | Synthesis of Ethyl 1-((1H-tetrazol-5-yl)methyl)-5-methyl-1H-pyrazole-3-carboxylate (HL4)

A suspension of sodium azide (0.29 g, 4.5 mmol), zinc chloride (0.61 g, 4.5 mmol) and ethyl 1-(cyanomethyl)-3-methyl-1H-pyrazole-5-carboxylate (0.58 g, 3 mmol) (**L3**) in water (60 mL) was heated to reflux for 5 h. After cooling to ambient temperature, the suspension was dissolved in 2 M hydrochloric acid (2 mL), resulting in the formation of a white precipitate, the desired product **HL4**. Yield: 67% (0.39 g). M. p.: >260°C. $^1$H NMR (300 MHz, DMSO-$d_6$, $\delta$ (ppm)): 6.53 (*d*, *J* = 0.7 Hz, 1H, $\boldsymbol{H}_{(pz)}$), 6.49 (s, 1H, $\boldsymbol{H}_{(ttrz)}$), 5.68 (s, 2H), 5.62 (s, C$\boldsymbol{H}_2$, 2H) 4.20 (*q*, *J* = 7.1 Hz, 2H, C$\boldsymbol{H}_{2\text{-}}CH_3$), 2.42 (s, 3H, C$\boldsymbol{H}_3$), 2.30 (*s*, 3H, C$\boldsymbol{H}_3$), 1.23 (*t*, *J* = 7.1 Hz, 3H, $CH_{2\text{-}}C\boldsymbol{H}_3$).

$^{13}$C NMR (75 MHz, DMSO-$d_6$, $\delta$ (ppm)): 161.8 (***C*** = O), 157.6 (1C, ***C***–$NH_{(ttrz)}$), 155.9, 141.5 (1C, ***C*** = $N_{(pz)}$), 141.1 (1C, ***C*** = $C_{(pz)}$), 108.0 (1C, $\boldsymbol{C}H_{(pz)}$), 60.1 (1C, $\boldsymbol{C}H_{2\text{-}}O$), 14.24 (1C, $\boldsymbol{C}H_{2(ttrz)}$), 10.89 (1C, $\boldsymbol{C}H_{3(pz)}$), 10.82 (1C, $\boldsymbol{C}H_{2\text{-}}CH_3$). FT-IR (KBr, cm$^{-1}$): 2849 (w), 2805 (w), 1585 (i), 1320 (w), 1089 (i). ESI-MS (+): *m/z* found = 237.10937, *m/z* calcd for [(HL4)+H]$^+$: 237.10945.

#### 4.3.5 | Synthesis of Coordination Compounds

$[Fe(\mathbf{L1})_3](ClO_4)_2$ (**1**) $[Co(\mathbf{L1})_3](ClO_4)_2$ (**2**) $[Ni(\mathbf{L1})_3](ClO_4)_2$ (**3**), $[Cu(\mathbf{L1})_2(NO_3)]NO_3$ (**4**), $[Cd(\mathbf{L1})(Cl)_2]_n$ (**5**).

CAUTION! Due to the potential explosiveness of metal perchlorate salts, only small quantities were handled with extreme care.

#### 4.3.6 | General Procedure

**L1** (60.6 mg, 0.3 mmol, 3 eq.) was dissolved in hot methanol (5 mL). To the vial containing this solution, a methanolic solution (5 mL) of $Fe(ClO_4)_2{\cdot}H_2O$ (25.47 mg, 0.1 mmol, 1eq.), $Co(ClO_4)_2{\cdot}6H_2O$ (36.59 mg, 0.1 mmol, 1 eq.), $Ni(ClO_4)_2{\cdot}6H_2O$ (36.56 mg, 0.1 mmol, 1eq.), $Cu(NO_3)_2{\cdot}3H_2O$, (24.16 mg, 0.1 mmol, 1eq.) or $CdCl_2{\cdot}H_2O$ (20.13 mg, 0.1 mmol, 1eq.) was added, respectively. The reaction mixture was stirred for 10 min at 60°C. X-ray diffraction-quality single crystals were obtained after 2 days *via* vapor diffusion of diethyl ether into the reaction mixture.

$[Fe(\mathbf{L1})_3](ClO_4)_2$ (**1**): Yield: 19.82 mg (23%). FT-IR (KBr, cm$^{-1}$): 3134 (w), 2932 (w), 2354 (w), 1596 (i), 1561 (m), 1087 (m). ESI-MS (+): *m/z* found = 330.1146, *m/z* calcd for $[Fe(\mathbf{L1})_3]^{2+}$: 330.1143. Anal. Calcd for $FeC_{27}H_{30}N_{18}Cl_2O_8$ (**1**): C, 37.65; H, 3.51; N, 29.27; O, 14.86. Found: C, 37.04; H, 3.26; N, 28.63; O, 15.39.

$[Co(\mathbf{L1})_3](ClO_4)_2$ (**2**): Yield: 37 mg (34%). FT-IR (KBr, cm$^{-1}$): 3137 (w), 2977 (w), 2348 (w), 1591 (i), 1562 (m), 1078 (m). ESI-MS (+): *m/z* found = 333.6111, *m/z* calcd for $[Co(\mathbf{L1})_3]^{2+}$: 333.6133. Anal. Calcd for $CoC_{27}H_{30}N_{18}Cl_2O_8$ (**2**): C, 37.51; H, 3.50; N, 29.16; O, 14.81. Found: C, 37.06; H, 3.31; N, 28.68; O, 15.17.

$[Ni(\mathbf{L1})_3](ClO_4)_2$ (**3**): Yield: 23.27 mg (27%). FT-IR (KBr, cm$^{-1}$): 3100 (w), 2926 (w), 2354 (w), 1597 (i), 1560 (m), 1092 (m). ESI-MS (+): *m/z* found = 332.1121, *m/z* calcd for $[Ni(\mathbf{L1})_3]^{2+}$: 332.1122. Anal.Calcd for $NiC_{27}H_{30}N_{18}Cl_2O_8$ (**3**): C, 37.52; H, 3.50; N, 29.17; O, 14.81. Found: C, 37.11; H, 3.22; N, 28.68; O, 15.26.

$[Cu(\mathbf{L1})_2(NO_3)]NO_3$ (**4**): Yield: 18.1 mg (21%). FT-IR (KBr, cm$^{-1}$): 3131 (w), 2932 (w), 2356 (w), 1597 (i), 1565 (m), 1377 (m). ESI-MS (+): *m/z* found = 467.1226, *m/z* calcd for $[Cu(\mathbf{L1})_2]^+$: 467.1224. Anal. Calcd for $CuC_{18}H_{20}N_{14}O_6$ (**4**): C, 36.52; H, 3.41; N, 33.12; O, 16.22. Found: C, 36.12; H, 3.22; N, 32.42; O, 16.50.

$[Cd(\mathbf{L1})Cl_2]_n$ (**5**): Yield : 17.24 mg (20%). FT-IR (KBr, cm$^{-1}$): 3131 (w), 2929 (w), 2354 (w), 1588 (i), 1562 (m). ESI-MS (+): *m/z* found = 427.1819, *m/z* calcd for ($[Cd(\mathbf{L1})Cl_2]$+MeCN+H)$^+$: 427.9705. Anal. Calcd for $CdC_9H_{10}N_6Cl_2$ (**5**): C, 28.04; H, 2.61; N, 21.80. Found: C, 27.80; H, 2.43; N, 21.20.

#### 4.3.7 | Synthesis of $[Ni(HL2)_3](ClO_4)_2$ (6)

**HL2** (73.5 mg, 0.3 mmol, 3 eq.) was dissolved in a 5% perchloric acid solution (2 mL) at ambient temperature. $Ni(ClO_4)_2{\cdot}6H_2O$ (36.56 mg, 1 mmol, 1 eq.) was dissolved in a 5% perchloric acid solution (1 mL) and added to the ligand solution, yielding a light purple solution. The mixture was stirred for 3 min. at 60°C and then allowed to crystallize under ambient conditions. After four days, small block-shaped light purple single crystals were formed, isolated by filtration and dried under ambient conditions. Yield: 34.56 mg (33%). FT-IR (KBr, cm$^{-1}$): 3134 (w), 2977 (w), 2354 (w), 1591 (i), 1520 (m), 1095 (m). ESI-MS (+): *m/z* found = 814.2516, *m/z* calcd for ($[Ni(\mathbf{HL2})(\mathbf{L2})_2]$+Na)$^+$: 814.2501. Anal. Calcd for $NiC_{27}H_{33}N_{27}Cl_2O_8{\cdot}3H_2O$ (**6**·$3H_2O$): C, 30.96; H, 3.75; N, 36.11; O, 16.80. Found: C, 30.55; H, 3.70; N, 35.62; O, 17.17.

#### 4.3.8 | Synthesis of $[Cu(HL2)Cl_2]_n$ (7)

At ambient temperature, **HL2** (24.51 mg, 0.1 mmol, 1 eq.) was dissolved in a 5% hydrochloric acid solution (3 mL). Copper(II) chloride (13.44 mg, 1 mmol, 1 eq.) was dissolved in a 5% hydrochloric acid solution (2 mL) and added to the ligand solution, resulting in a dark green solution. The mixture was stirred for 3 min. at 60°C before being allowed to crystallize. After three days, small dark green single crystals were formed, isolated by filtration and dried under ambient conditions. Yield: 9.45 mg (25%). FT-IR (KBr, cm$^{-1}$): 3103 (w), 1597 (i), 1511 (m). ESI-MS (−): *m/z* found = 378.9718, *m/z* calcd. for ($[Cu(\mathbf{HL2})Cl_2]$+H)$^-$: 378.9894. Anal. Calcd for $Cu_2C_{18}H_{22}N_{18}Cl_3$ (**7**): C, 29.86; H, 3.06; N, 34.83. Found : C, 30.38; H, 3.10; N, 35.32.

#### 4.3.9 | Synthesis of $[Co(MeOH)_2(L3)_2](ClO_4)_2$ (8)

**L3** (57.9 mg, 0.3 mmol, 3 eq.) in methanol (2.5 mL) was slowly added to a methanolic solution (2.5 mL) of $Co(ClO_4)_2{\bullet}6H_2O$ (36.59 mg, 0.1 mmol, 1 eq.). The resulting solution was stirred

for 10 min. at 60°C. The reaction mixture was then left under vapor diffusion of diethyl ether, and after five days, brick-orange single crystals were obtained. Yield: 19.83 mg (28%). FT-IR (KBr, $cm^{-1}$): 2957 (w), 1707 (i), 1221 (i), 1120 (w). ESI-MS (+): *m/z* found = 222.5512, *m/z* calcd. for $[Co(\mathbf{L2})_2]^{2+}$ = 222.5512; *m/z* found = 319.0938, *m/z* calcd. for $[Co(\mathbf{L2})_3]^{2+}$ = 319.0937; *m/z* found = 544.0522, *m/z* calcd. for $[Co(\mathbf{L2})_2(ClO_4)]^+$ = 544.0514. Anal. Calcd for $CoC_{19}H_{26}N_6ClO_{13}•2H_2O$ ($[Co(MeOH)(\mathbf{L3})_2](ClO_4)_2•2H_2O$): C, 31.59; H, 3.79; N, 12.00. Found: C, 32.04; H, 4.25; N, 11.80.

#### 4.3.10 | Synthesis of $[Cu(MeCN)_2(L3)_2](ClO_4)_2$ (9)

**L3** (57.9 mg, 0.2 mmol, 3 eq.) was dissolved in hot acetonitrile (5 mL) and then added to a solution of $Cu(ClO_4)_2•6H_2O$ (37.05 mg, 0.1 mmol, 1 eq.) in acetonitrile. The reaction mixture was stirred for 10 min. at 60°C. Clear blue single crystals were obtained after four days by vapor diffusion of diethyl ether into the reaction mixture. Yield: 13.88 mg (19%). FT-IR (KBr, $cm^{-1}$): 2983 (w), 1683 (i), 1282 (i), 1097 (i). ESI-MS (+): *m/z* found = 224.5499, *m/z* calcd. for $[Cu(\mathbf{L3})_2]^{2+}$: 224.5494; *m/z* found = 354.9629, *m/z* calcd. for $[Cu(\mathbf{L3})(ClO_4)]^+$: 354.9632; *m/z* found = 548.0475, *m/z* calcd. for $[Cu(\mathbf{L3})_2(ClO_4)]^+$: 548.0484. Anal. Calcd for $CuC_{22}H_{28}N_8Cl_2O_{12}•HClO_4•3H_2O$ (**9**•$HClO_4•3H_2O$): C, 29.84; H, 3.98; N, 12.66. Found: C, 29.45; H, 3.78; N, 11.35.

#### 4.3.11 | Synthesis of $\{[Cu(HL4')_2]·2H_2O\}_n$ (10)

**HL4** (70.86 mg, 0.3 mmol, 3 eq.) was dissolved in 5% perchloric acid (2 mL) at ambient temperature. $Cu(ClO_4)_2•6H_2O$ (37.05 mg, 0.1 mmol, 1 eq.), dissolved in the same acid (1 mL), was then added to the reaction mixture, resulting in a light blue solution. The mixture was stirred for 3 min. at 60°C, then allowed to crystallize. After two days, small light-blue single crystals were obtained. Yield: 16.57 mg (31%). FT-IR (KBr, $cm^{-1}$): 3117 (w), 3003 (w), 1605 (i), 1431 (i), 1310 (i).

#### 4.3.12 | Synthesis of $[Cu(HL4')Cl]_n$ (11)

**HL4** (70.86 mg, 0.3 mmol, 3 eq.) was dissolved in 5% hydrochloric acid (2 mL) at ambient temperature. Copper(II) chloride (13.44 mg, 0.1 mmol, 1 eq.) was dissolved in 5% hydrochloric acid (1 mL) and then added to the reaction mixture, resulting in the formation of a dark blue solution. The solution was stirred for 3 min. at 60°C and then left to crystallize. Small, dark-blue, well-formed crystals were isolated after two days. Yield: 7.65 mg (25%). FT-IR (KBr, $cm^{-1}$): 3123(w), 2972(m), 1645(i), 1443(i), 1252(i). ESI-MS (+): *m/z* found = 269.9923, *m/z* calcd. for $[Cu(\mathbf{L4'})]^+$: 269.9926. ESI-MS (−): *m/z* found = 476.0516, *m/z* calcd. for $[Cu(\mathbf{HL4'})(\mathbf{L4'})]$–: 476.0479; *m/z* found = 307.0214, *m/z* calcd. for $[Cu(\mathbf{L4'})Cl]^-$: 307.1770.

#### 4.3.13 | Synthesis of $[Ni(L5)_3](ClO_4)_2$ (12)

It was synthesized following the literature procedure.[80]

#### 4.3.14 | Synthesis of $[Ni(HL6)(L6)](ClO_4)$ (13)

**HL6** (51.6 mg, 0.2 mmol, 2 eq.) was dissolved in 5% perchloric acid (3 mL) at ambient temperature. $Ni(ClO_4)_2•6H_2O$ (37 mg, 0.1 mmol, 1 eq.) was dissolved in 5% perchloric acid (2 mL) and immediately added to **HL6**, resulting in the formation of a purple powder. Yield: 19.5 mg (29%). FT-IR (KBr, $cm^{-1}$): 3164(w), 2927(w), 2351(w), 1555(i), 1072(i). ESI-MS (+): *m/z* found = 287.1010, *m/z* calcd. for $[Ni(\mathbf{HL6})_2]^{2+}$: 287.1013; *m/z* found = 573.1953, *m/z* calcd. for $[Ni(\mathbf{HL6})(\mathbf{L6})]^+$: 573.1953; *m/z* found = 595.1768, *m/z* calcd. for $([Ni(L6)_2]+Na)^+$: 595.1772. ESI-MS (−): *m/z* found = 607.1575, *m/z* calcd. for $[Ni(\mathbf{L6})_2]Cl^-$: 607.1574. Anal. Calcd for **13**·$HClO_4·3H_2O$ ($NiC_{22}H_{27}N_{16}ClO_4·HClO_4·3H_2O$): C, 31.91; H, 4.14; N, 27.06; O, 21.25. Found: C, 32.37; H, 3.87; N, 26.77; O, 20.92.

#### 4.3.15 | Synthesis of $[Ni_2(HL6)(L6)Cl_3]$ (14)

A solution of **HL6** (51.6 mg, 0.2 mmol, 2 eq.) in 5% hydrochloric acid (3 mL) was added slowly to 5% hydrochloric acid (2 mL) of $NiCl_2•6H_2O$ (23.7 mg, 0.1 mmol, 1 eq.). The resulting solution was stirred for 5 min at 60°C. The reaction mixture was left for slow evaporation, and purple single crystals were obtained by filtration after one week. Yield: 20 mg (27%). FT-IR (KBr, $cm^{-1}$): 3147(w), 2916(w), 2351(w), 1552(i). ESI-MS (+): *m/z* found = 287.1011, m/z calcd. for $[Ni(\mathbf{HL6})_2]^{2+}$: 287.1013; *m/z* found = 573.1955, *m/z* calcd. for $[Ni(\mathbf{HL6})(\mathbf{L6})]^+$: 573.1953. ESI-MS (−): *m/z* found = 607.1575, *m/z* calcd. for $[Ni(L6)_2]Cl$–: 607.1574. Anal. Calcd for **14**·$H_2O$ ($Ni_2C_{22}H_{27}N_{16}Cl_3·H_2O$): C, 34.89; H, 3.86; N, 29.59; O, 2.11. Found: C, 34.67; H, 3.67; N, 29.08; O, 2.21.

#### 4.3.16 | Cytotoxicity Test

CH1 cells (provided by L. R. Kelland, CRC Centre for Cancer Therapeutics, Institute of Cancer Research, Sutton, UK; identified as PA-1 (RRID:CVCL_0479) ovarian teratocarcinoma cells by STR profiling at Multiplexion, Heidelberg, Germany), SW480 (RRID:CVCL_0546) colon carcinoma and A549 (RRID:CVCL_0023) lung adenocarcinoma cells (both obtained from the American Type Culture Collection (ATCC), Manassas, VA, USA) were grown as adherent cultures in 75 $cm^2$ culture flasks (Starlab, Hamburg, Germany) in minimal essential medium (MEM) supplemented with 1 mM sodium pyruvate, 4 mM L-glutamine, 1% v/v nonessential amino acids from 100-fold solution (all purchased from Sigma–Aldrich, St. Louis, MO, USA) and 10% v/v heat-inactivated fetal bovine serum (Serana, Pessin, Germany) under 5% $CO_2$ in air at 37°C.

Cytotoxicity of the compounds was determined by the MTT (3-(4,5-dimethylthiazol-2-yl)-2,5-diphenyl-2H tetrazolium bromide, Acros Organics, Geel, Belgium) assay. For this purpose, cells were harvested by trypsinization, seeded in 100 μL aliquots into 96-well flat-bottom microculture plates (Starlab, UK) in densities of $1 \times 10^3$ (CH1/PA-1), $2 \times 10^3$ (SW480) and $3 \times 10^3$ (A549) cells per well, and incubated for 24 h for readherence and resuming of exponential proliferation. Test compounds were diluted in 99.8% pure DMF (Honeywell/Riedel-de-Haën, Seelze, Germany), serially diluted in MEM (not to exceed a maximum of 0.5% *v*/*v* DMF in test plates), and added to the plates in aliquots

of 100 µL per well. After continuous exposure for 72 h, the medium was replaced with 100 µL of a medium/MTT mixture [6 parts of RPMI 1640 medium (Sigma–Aldrich) supplemented with 10% heat-inactivated fetal bovine serum and 2 mM L-glutamine; 1 part of MTT solution in phosphate buffered saline (5 mg $mL^{-1}$)]. After incubation for 4 h, the medium/MTT mixture was removed, and produced formazan crystals were dissolved in 150 µL DMSO (Fisher Scientific, Waltham, MA, USA) per well. Optical densities at 550 nm (and a reference wavelength of 690 nm) were measured with an ELx808 microplate reader (Bio-Tek, Winooski, VT, USA). The 50% inhibitory concentrations ($IC_{50}$) were interpolated from concentration–effect curves of three independent tests, each comprising triplicates per concentration level. In case of inactivity, at least two independent tests were performed.

## Author Contributions

YB performed synthesis and wrote the paper with YD, YG, MAJ and MW. SR and YG both designed and managed the project. YD run some experiments. HNM, KR and MF undertook X-ray studies. OC performed the Hirshfeld analysis of the crystal structures. YB, MW and OC carried out characterization of samples. AR performed magnetic measurements and WL Mössbauer measurements. HB performed the cytotoxicity tests.

## Acknowledgments

This research was supported by a bilateral WBI-Morocco grant (2018–2022), the Fonds de la Recherche Scientifique-FNRS (PDR T.0095.21, CDR J.0064.23, CDR J.0168.22, EQP U.N027.24), the PPR2-MESRSFC-CNRSTP10 project (Morocco), University of Glasgow and the UEFISCDI (HighSensSpin, TE 77 / 2022 (PN-III-P1-1.1-TE-2021-1654). We thank CNRST Morocco and WBI Morocco for an excellence PhD stipendium as well as the ARES for a PhD scholarship allocated to YB. W. L. was supported by fellowship from the China Scholarship Council (201908310083). The authors gratefully acknowledge the Mass Spectrometry Center and the Core Facility for Crystal Structure Analysis, Faculty of Chemistry, University of Vienna. We also thank Michaela Hejl (Institute of Inorganic Chemistry, University of Vienna) for cytotoxicity tests of reference compounds.

## Conflicts of Interest

There are no conflicts to declare.

## Data Availability Statement

The data that support the findings of this study are available from the corresponding author upon reasonable request.

## References

1. Z. H. Chohan and S. H. Sumrra, "Synthesis, Characterization and Biological Properties of Thienyl Derived Triazole Schiff Bases and Their Oxovanadium(IV) Complexes," *Journal of Enzyme Inhibition and Medicinal Chemistry* 27 (2012): 187–193, https://doi.org/10.3109/14756366.2011.582686.

2. G. Aromí, L. A. Barrios, O. Roubeau, and P. Gamez, *Coordination Chemistry Reviews* 255 (2011): 485–546.

3. H. Benaissa, M. Wolff, K. Robeyns, et al., "Syntheses, Crystal Structures, Luminescent Properties, and Electrochemical Synthesis of Group 12 Element Coordination Polymers with 4-Substituted 1,2,4-Triazole Ligands," *Crystal Growth & Design* 19 (2019): 5292–5307, https://doi.org/10.1021/acs.cgd.9b00734.

4. Y. Boland, B. Tinant, D. A. Safin, J. Marchand-Brynaert, R. Clerac, and Y. Garcia, "A Metal–organic Framework Made of an Asymmetric 1,2,4-triazole and Tetrazole Ligand," *CrystEngComm* 14 (2012): 8153–8155, https://doi.org/10.1039/c2ce26257f.

5. S. Radi, M. El-Massaoudi, H. Benaissa, et al., "Crystal Engineering of a Series of Complexes and Coordination Polymers Based on Pyrazole-carboxylic Acid Ligands," *New Journal of Chemistry* 41 (2017): 8232–8241, https://doi.org/10.1039/C7NJ01714F.

6. Y. Garcia, N. Adarsh, and A. D. Naik, "Crystal Engineering of FeII Spin Crossover Coordination Polymers Derived From Triazole or Tetrazole Ligands," *Chimia* 67 (2013): 411–411, https://doi.org/10.2533/chimia.2013.411.

7. Y. Garcia, *Advances in Inorganic Chemistry* 76 (2020): 121–153.

8. B. Benaicha, K. Van Do, A. Yangui, et al., "Interplay Between Spin-crossover and Luminescence in a Multifunctional Single Crystal Iron( ii ) Complex: towards a New Generation of Molecular Sensors," *Chemical Science* 10 (2019): 6791–6798, https://doi.org/10.1039/C9SC02331C.

9. K. Chkirate, S. Fettach, M. El Hafi, et al., "Solvent Induced Supramolecular Polymorphism in Cu(II) Coordination Complex Built From 1,2,4-triazolo[1,5-a]Pyrimidine: Crystal Structures and Anti-oxidant Activity," *Journal of Inorganic Biochemistry* 208 (2020): 111092, https://doi.org/10.1016/j.jinorgbio.2020.111092.

10. Y. Sicak, "Design and Antiproliferative and Antioxidant Activities of Furan-based Thiosemicarbazides and 1,2,4-triazoles: Their Structure-activity Relationship and SwissADME Predictions," *Medicinal Chemistry Research* 30 (2021): 1557–1568, https://doi.org/10.1007/s00044-021-02756-z.

11. S. Q. Wang, Y. F. Wang, and Z. Xu, "Tetrazole Hybrids and Their Antifungal Activities," *European Journal of Medicinal Chemistry* 170 (2019): 225–234, https://doi.org/10.1016/j.ejmech.2019.03.023.

12. R. S. Upadhayaya, N. Sinha, S. Jain, N. Kishore, R. Chandra, and S. K. Arora, *Medicinal Chemistry* 12 (2004): 2225–2238.

13. A. Alrubaye, *Al-Nahrain J Sci* 25 (2022): 8–13.

14. W. Zafar, S. H. Sumrra, and Z. H. Chohan, "A Review: Pharmacological Aspects of Metal Based 1,2,4-triazole Derived Schiff Bases," *European Journal of Medicinal Chemistry* 222 (2021): 113602, https://doi.org/10.1016/j.ejmech.2021.113602.

15. M. J. Kharodawala and A. K. Rana, "Synthesis, Characterization, and Biological Activity of some Transition Metal Chelates of 4-Acyloxime-2-Pyrazolin-5-Ones," *Synthesis and Reactivity in Inorganic and Metal-Organic Chemistry* 33 (2003): 1483–1504, https://doi.org/10.1081/SIM-120024324.

16. P. Banerjee, O. P. Pandey, and S. K. Sengupta, "Microwave Assisted Synthesis, Spectroscopic and Antibacterial Studies of Titanocene Chelates of Schiff Bases Derived From 3-substituted-4-amino-5-hydrazino-1,2,4-triazoles," *Transition Metal Chemistry* 33 (2008): 1047–1052, https://doi.org/10.1007/s11243-008-9152-1.

17. A. Fouda, M. El-Morsi, M. Gaber, and M. Fakeeh, "A Comparative Study of the Corrosion Inhibition of Carbon Steel in HCl Solution by 1-[(5-mercapto-1H-1,2,4-triazole-3-yl) diazenyl] Naphthalene-2-Ol (HL) and Its Manganese Complex," *Chemical Data Collections* 28 (2020): 100479, https://doi.org/10.1016/j.cdc.2020.100479.

18. M. Nasrollahzadeh, Z. Nezafat, N. S. S. Bidgoli, and N. Shafiei, *Molecular Catalysis* 513 (2021): 111788.

19. L. Sun, A. Rotaru, K. Robeyns, and Y. Garcia, "A Colorimetric Sensor for the Highly Selective, Ultra-sensitive, and Rapid Detection of Volatile Organic Compounds and Hazardous Gases," *Industrial & Engineering Chemistry Research* 60 (2021): 8788–8798, https://doi.org/10.1021/acs.iecr.1c01389.

20. L. Sun, A. Rotaru, and Y. Garcia, "A Non-porous Fe(II) Complex for the Colorimetric Detection of Hazardous Gases and the Monitoring of Meat Freshness," *Journal of Hazardous Materials* 437 (2022): 129364, https://doi.org/10.1016/j.jhazmat.2022.129364.

21. D. Shi, C. Cui, S. Wang, et al., "Tetrazole-Containing Triphenylamine-Based MOF as a Sensitive Sensor for Food Inspection," *Inorganic Chemistry* 61 (2022): 13768–13774, https://doi.org/10.1021/acs.inorgchem.2c01456.

22. Y. Chi, B. Tong, and P. T. Chou, "Metal Complexes with Pyridyl Azolates: Design, Preparation and Applications," *Coordination Chemistry Reviews* 281 (2014): 1–25, https://doi.org/10.1016/j.ccr.2014.08.012.

23. J. P. Zhang, Y. B. Zhang, J. B. Lin, and X. M. Chen, "Metal Azolate Frameworks: from Crystal Engineering to Functional Materials," *Chemical Reviews* 112 (2012): 1001–1033, https://doi.org/10.1021/cr200139g.

24. R. K. Uppadhayay, A. Kumar, J. Teotia, and A. Singh, "Multifaceted Chemistry of Tetrazole. Synthesis, Uses, and Pharmaceutical Applications," *Russian Journal of Organic Chemistry* 58 (2022): 1801–1811, https://doi.org/10.1134/S1070428022120090.

25. S. Khan, T. Iqbal, M. B. Khan, R. Hussain, Y. Khan, and H. W. Darwish, "Novel Pyrrole Based Triazole Moiety as Therapeutic Hybrid: Synthesis, Characterization, and Anti-Alzheimer Potential with Molecular Mechanism of Protein Ligand Profile," *BMC Chemistry* 18 (2024): 223, https://doi.org/10.1186/s13065-024-01340-x.

26. N. Hura, A. Naaz, S. S. Prassanawar, S. K. Guchhait, and D. Panda, "Drug-Clinical Agent Molecular Hybrid: Synthesis of Diaryl(trifluoromethyl)Pyrazoles as Tubulin Targeting Anticancer Agents," *ACS Omega* 3 (2018): 1955–1969, https://doi.org/10.1021/acsomega.7b01784.

27. A. A. Gaber, A. M. El-Morsy, F. F. Sherbiny, et al., *Archiv Der Pharmazie* 358 (2021): e2100258.

28. M. Ghorbanpour, B. Soltani, A. Mota, et al., "Copper (II) Complexes with N, S Donor Pyrazole-based Ligands as Anticancer Agents," *Biometals* 35 (2022): 1095–1111, https://doi.org/10.1007/s10534-022-00426-0.

29. B. Nagaraju, J. Kovvuri, C. G. Kumar, et al., "Synthesis and Biological Evaluation of Pyrazole Linked Benzothiazole-$\beta$-naphthol Derivatives as Topoisomerase I Inhibitors with DNA Binding Ability," *Bioorganic & Medicinal Chemistry* 27 (2019): 708–720, https://doi.org/10.1016/j.bmc.2019.01.011.

30. S. Z. Ren, Z. C. Wang, D. Zhu, et al., "Design, Synthesis and Biological Evaluation of Novel Ferrocene-pyrazole Derivatives Containing Nitric Oxide Donors as COX-2 Inhibitors for Cancer Therapy," *European Journal of Medicinal Chemistry* 157 (2018): 909–924, https://doi.org/10.1016/j.ejmech.2018.08.048.

31. G. M. Nitulescu, G. Stancov, O. C. Seremet, et al., "The Importance of the Pyrazole Scaffold in the Design of Protein Kinases Inhibitors as Targeted Anticancer Therapies," *Molecules (Basel, Switzerland)* 28 (2023): 5359, https://doi.org/10.3390/molecules28145359.

32. Y. Zhang, C. Wu, N. Zhang, R. Fan, Y. Ye, and J. Xu, "Recent Advances in the Development of Pyrazole Derivatives as Anticancer Agents," *International Journal of Molecular Sciences* 24 (2023): 12724, https://doi.org/10.3390/ijms241612724.

33. Y. Deswal, S. Asija, D. Kumar, et al., *Research on Chemical Intermediates* (2022): 27.

34. C. Sonkar, N. Malviya, N. Sinha, A. Mukherjee, S. Pakhira, and S. Mukhopadhya, "Selective Anticancer Activities of Ruthenium(II)-tetrazole Complexes and Their Mechanistic Insights," *Biometals* 34 (2021): 795–812, https://doi.org/10.1007/s10534-021-00308-x.

35. Y. Draoui, S. Radi, Y. Bahjou, et al., *RSC Advances* 13 (2023): 36158–36167.

36. C. Sonkar, N. Malviya, N. Sinha, A. Mukherjee, S. Pakhira, and S. Mukhopadhyay, "Selective Anticancer Activities of Ruthenium(II)-tetrazole Complexes and Their Mechanistic Insights," *Biometals* 34 (2021): 795–812, https://doi.org/10.1007/s10534-021-00308-x.

37. D. L. Lewis, E. D. Estes, and D. J. Hodgson, "The Infrared Spectra of Coordinated Perchlorates," *Journal of Crystal and Molecular Structure* 5 (1975): 67–74, https://doi.org/10.1007/BF01202553.

38. M. Y. Mihaylov, V. R. Zdravkova, E. Z. Ivanova, et al., "Infrared Spectra of Surface Nitrates: Revision of the Current Opinions Based on the Case Study of Ceria," *Journal of Catalysis* 394 (2021): 245–258, https://doi.org/10.1016/j.jcat.2020.06.015.

39. Y. Garcia, C. M. Grunert, S. Reiman, O. van Campenhoudt, and P. Gütlich, "The Two-Step Spin Conversion in a Supramolecular Triple Helicate Dinuclear Iron(II) Complex Studied by Mössbauer Spectroscopy," *European Journal of Inorganic Chemistry* 2006 (2006): 3333–3339, https://doi.org/10.1002/ejic.200600365.

40. M. El-Massaoudi, S. Radi, A. Salhi, et al., "Novel 1D Coordination Polymers Built From Acyclic Cryptate Containing Bis(1 H -1,2,4-triazole) Ligands and Featuring Coordinated Counteranions," *New Journal of Chemistry* 42 (2018): 11324–11333, https://doi.org/10.1039/C8NJ00799C.

41. C. Tanaka, K. Kuratani, and S. I. Mizushima, "In-plane Normal Vibrations of Methanol," *Spectrochimica Acta* 9 (1957): 265–269, https://doi.org/10.1016/0371-1951(57)80141-6.

42. J. R. Durig, K. L. Hellams, and J. H. Mulligan, "Vibrational Spectra and Structure of Some Silicon Containing Compounds—IV," *Spectrochimica Acta Part A: Molecular Spectroscopy* 28 (1972): 1039–1057, https://doi.org/10.1016/0584-8539(72)80076-X.

43. P. Guionneau, "Crystallography and Spin-crossover. A View of Breathing Materials," *Dalton Transactions* 43 (2014): 382–393, https://doi.org/10.1039/C3DT52520A.

44. S. Xue, Y. Guo, and Y. Garcia, "Spin Crossover Crystalline Materials Engineered via Single-crystal-to-single-crystal Transformations," *CrystEngComm* 23 (2021): 7899–7915, https://doi.org/10.1039/D1CE00234A.

45. L. G. Lavrenova and O. G. Shakirova, "Spin Crossover and Thermochromism of Iron(II) Coordination Compounds With 1,2,4-Triazoles and Tris(pyrazol-1-yl)Methanes," *European Journal of Inorganic Chemistry* 2013 (2013): 670–682, https://doi.org/10.1002/ejic.201200980.

46. G. J. Kleywegt, W. G. R. Wiesmeijer, G. J. Van Driel, W. L. Driessen, J. Reedijk, and J. H. Noordik, "Unidentate versus Symmetrically and Unsymmetrically Bidentate Nitrate co-ordination in Pyrazole-containing Chelates. The Crystal and Molecular Structures of (nitrato-O)[tris(3,5-dimethylpyrazol-1-ylmethyl)amine]Copper( II ) Nitrate, (nitrato-O,O′)[tris(3,5-dimethylpyrazol-1-ylmethyl)amine]Nickel( II ) Nitrate, and (nitrato-O)(nitrato-O,O′)[tris(3,5-dimethylpyrazol-1-ylmethyl)amine]Cadmium( II )," *Journal of the Chemical Society, Dalton Transactions* (1985): 2177, https://doi.org/10.1039/DT9850002177.

47. A. W. Addison, T. N. Rao, J. Reedijk, J. van Rijn, and G. C. Verschoor, *Journal of the Chemical Society, Dalton Transactions* (1984): 1349–1356.

48. T. Neumann, B. C. Thompson, D. Hebron, et al., "Heterobimetallic 3d–4f Complexes Supported by a Schiff-base Tripodal Ligand," *Dalton Transactions* 53 (2024): 9921–9932, https://doi.org/10.1039/D3DT03760F.

49. G. G. Nnabuike, S. Salunke-Gawali, A. S. Patil, et al., "Copper(II) Complexes Containing Derivative of Aminobenzoic Acid and Nitrogen-rich Ligands: Synthesis, Characterization and Cytotoxic Potential," *Journal of Molecular Structure* 1279 (2023): 135002, https://doi.org/10.1016/j.molstruc.2023.135002.

50. P. Agarwal, A. Kumar, I. Verma, et al., "The Reversible Interconversion of Copper( ii ) Dimers Bearing Phenolate-based Ligands in Their Monomers: Theoretical and Experimental Viewpoints," *New Journal of Chemistry* 45 (2021): 1203–1215, https://doi.org/10.1039/D0NJ00484G.

51. A. M. Lopez_Marzo, M. Guerrero, T. Calvet, M. Font-Bardia, and J. Pons, "Structural Characterization of a New Polymeric Cu(II) Complex With Unexpected Chlorinated Pyrazole Ligand," *Inorganic Chemistry Communications* 55 (2015): 51, https://doi.org/10.1016/j.inoche.2015.03.001.

52. T. R. G. Simoes, R. V. Mambrini, D. O. Reis, et al., "Copper(ii) Assembling With Bis(2-pyridylcarbonyl)Amidate and N,N′-2,2-phenylenebis(oxamate)," *Dalton Transactions* 42 (2013): 5778, https://doi.org/10.1039/c3dt32949f.

53. Y. Chen, J. Wu, S. Ma, et al., *Journal of Molecular Structure* 1089 (2015): 1–8.

54. Y. M. Zhao, G. M. Tang, Y. T. Wang, Y. Z. Cui, and S. W. Ng, "Copper-based Metal Coordination Complexes With Voriconazole Ligand: Syntheses, Structures and Antimicrobial Properties," *Journal of Solid State Chemistry* 259 (2018): 19–27, https://doi.org/10.1016/j.jssc.2017.12.029.

55. A. A. Recio Despaigne, F. B. Da Costa, O. E. Piro, E. E. Castellano, S. R. W. Louro, and H. Beraldo, "Complexation of 2-acetylpyridine- and 2-benzoylpyridine-derived Hydrazones to Copper(II) as an Effective Strategy for Antimicrobial Activity Improvement," *Polyhedron* 38 (2012): 285, https://doi.org/10.1016/j.poly.2012.03.017.

56. D. Q. Feng, X. P. Zhou, J. Zheng, G. H. Chen, X. C. Huang, and D. Li, "In Situ Selective N-alkylation of Pendant Pyridyl Functionality in Mixed-valence Copper Complexes With Methanol and Copper(ii) Bromide," *Dalton Transactions* 41 (2012): 4255, https://doi.org/10.1039/c2dt12081j.

57. M. Magini, "Coordination of Copper(II). Evidence of the Jahn-Teller Effect in Aqueous Perchlorate Solutions," *Inorganic Chemistry* 21 (1982): 1535–1538, https://doi.org/10.1021/ic00134a053.

58. Y.-Q. Wang, W.-H. Bi, X. Li, and R. Cao, "(2,2′-Bipyridine-$\kappa$ 2N, N ′)dichlorocopper(II)," *Acta Crystallographica Section E Structure Reports Online* 60 (2004): m876–, https://doi.org/10.1107/S1600536804012565.

59. M. Hernández-Molina, J. González-Platas, C. Ruiz-Pérez, F. Lloret, and M. Julve, "Crystal Structure and Magnetic Properties of the Single-$\mu$-chloro Copper(II) Chain [Cu(bipy)Cl2] (bipy = 2,2′-bipyridine)," *Inorganica Chimica Acta* 284 (1999): 258, https://doi.org/10.1016/S0020-1693(98)00300-4.

60. P. R. Spackman, M. J. Turner, J. J. McKinnon, et al., "CrystalExplorer : A Program for Hirshfeld Surface Analysis, Visualization and Quantitative Analysis of Molecular Crystals," *Journal of Applied Crystallography* 54 (2021): 1006–1011, https://doi.org/10.1107/S1600576721002910.

61. C. B. Pinto, L. H. Dos Santos, and B. L. Rodrigues, "Understanding Metal–ligand Interactions in Coordination Polymers Using Hirshfeld Surface Analysis," *Acta Crystallographica Section C Structural Chemistry* 75 (2019): 707–716, https://doi.org/10.1107/S2053229619005874.

62. K. Lagarec and D. G. Rancourt, University of Ottawa, ON (1998).

63. CrysAlisPro, version 1.171.33.49b, Oxford Diffraction Ltd., Abingdon, UK (2009), http://www.ccdc.cam.ac.uk/structures">Access.

64. G. M. Sheldrick, *Acta Crystallographica* A71 (2015): 3–8.

65. G. M. Sheldrick, *Acta Crystallographica* C71 (2015): 3–8.

66. A. L. Spek, *Acta Crystallographica* C71 (2015): 9–18.

67. G. M. Sheldrick, "Phase Annealing in SHELX-90: Direct Methods for Larger Structures," *Acta Crystallographica Section A Foundations of Crystallography* 46 (1990): 467–473, https://doi.org/10.1107/S0108767390000277.

68. G. M. Sheldrick, "A Short History of SHELX," *Acta Crystallographica Section A Foundations of Crystallography* 64 (2008): 112–122, https://doi.org/10.1107/S0108767307043930.

69. L. J. Farrugia, "WinGX Suite for Small-molecule Single-crystal Crystallography," *Journal of Applied Crystallography* 32 (1999): 837–838, https://doi.org/10.1107/S0021889899006020.

70. R. Clark and J. Reid, "The Analytical Calculation of Absorption in Multifaceted Crystals," *Acta Crystallographica Section A Foundations of Crystallography* 51 (1995): 887–897, https://doi.org/10.1107/S0108767395007367.

71. A. Altomare, G. Cascarano, C. Giacovazzo, and A. Guagliardi, "Completion and Refinement of Crystal Structures With SIR 92," *Journal of Applied Crystallography* 26 (1993): 343–350, https://doi.org/10.1107/S0021889892010331.

72. Crystal Structure 4.2: Crystal Structure Analysis Package, Rigaku Corporation (2000-2015). Tokyo 196–8666, Japan, http://www.ccdc.cam.ac.uk/structures">Access.

73. O. V. Dolomanov, J. L, R. J. G. Bourhis, J. A. K. Howard, and H. Puschmann, "OLEX2 : A Complete Structure Solution, Refinement and Analysis Program," *Journal of Applied Crystallography* 42 (2009): 339–341, https://doi.org/10.1107/S0021889808042726.

74. C. B. Huebschle, G. M. Sheldrick, and B. Dittrich, "ShelXle: a Qt Graphical User Interface for SHELXL," *Journal of Applied Crystallography* 44 (2011): 1281–1284, https://doi.org/10.1107/S0021889811043202.

75. G. M. Sheldrick, SHELXS v 2016/4, University of Göttingen (2015).

76. G. M. Sheldrick, SHELXL v 2016/4, University of Göttingen (2015).

77. A. L. Spek, *Acta Crystallographica* 65 (2009): 148–155.

78. Y. Draoui, S. Radi, M. El-Massaoudi, et al., "Coordination Complexes Built From a Ditopic Triazole-Pyrazole Ligand With Antibacterial and Antifungal Performances," *Molecules (Basel, Switzerland)* 28 (2023): 6801, https://doi.org/10.3390/molecules28196801.

79. Y. Bahjou, S. Radi, M. El Massaoudi, et al., *European Journal of Inorganic Chemistry* 27 (2024): e202300634.

## Supporting Information

Additional supporting information can be found online in the Supporting Information section.

**Supporting file 1**: chem70667-sup-0001-SuppMat.docx **Supporting file 2**: chem70667-sup-0002-Data.zip